Photoemission in the NO molecular frame induced by soft-x-ray elliptically polarized light above the $N(1s)^{-1}$ and $O(1s)^{-1}$ ionization thresholds

W. B. Li,[1,*] R. Montuoro,[3] J. C. Houver,[1] L. Journel,[2] A. Haouas,[2] M. Simon,[2] R. R. Lucchese,[3] and D. Dowek[1]
[1]*Laboratoire des Collisions Atomiques et Moléculaires (UMR 8625 UPS-CNRS), Bâtiment 351, Université Paris-Sud, 91405 Orsay, France*
[2]*Laboratoire de Chimie Physique-Matière et Rayonnement (UMR 7614 UPMC-CNRS), 11 rue Pierre et-Marie Curie, 75231 Paris Cedex 05, France*
[3]*Department of Chemistry, Texas A&M University, College Station, Texas 77843-3255, USA*
(Received 1 February 2007; published 25 May 2007)

Complete experiments in inner-shell photoionization of linear molecules are achieved by combining the velocity vector correlation method, based on imaging and time-of-flight-resolved electron-ion-ion coincidence technique, with the use of elliptically polarized light. We report here on the molecular frame photoelectron angular distributions (MFPADs) obtained using this method in a single experiment performed with elliptically polarized light, for a site selective *K*-shell ionization of the NO molecule in the region of the $N(1s)^{-1}$ and $O(1s)^{-1}$ shape resonances. For a comparable photoelectron energy the $N(1s)^{-1}$ and $O(1s)^{-1}$ MFPADs display a remarkable symmetry in the inversion with respect to the emission center of the NO molecule, while revealing common features such as, in particular, the dominant role of *p* and *f* partial-wave channels in the photoelectron emission. A large molecular frame circular dichroism is observed. These results are well predicted by multichannel Schwinger configuration interaction calculations (MCSCI), which provide additional information for $NO^+(^3\Pi)$ and $NO^+(^1\Pi)$ multiplet specific photoionization reactions. The analysis of the photoelectron-ion-ion kinetic energy correlation characterizes the ionic fragmentation channels populated after Auger decay of the $NO^+(1s_{N/O})^{-1}$ ionic states.

DOI: 10.1103/PhysRevA.75.052718 PACS number(s): 33.80.Eh

I. INTRODUCTION

The vector correlation (VC) method [1] previously developed for the detailed study of dissociative valence-shell photoionization of molecules induced by linearly [2,3] and circularly [4] polarized light has been extended to investigate inner-shell photoionization processes. With the VC method, we mean both the experimental method involving ion-electron three-dimensional velocity imaging of the dissociative photoionization (DPI) events collected in a large acceptance solid angle, and the theory of measurements based on a unified analytical description of the molecular frame photoelectron angular distribution (MFPAD) characterizing the photoionization reaction [1–4]. In this paper we report on recent results about *K*-shell photoionization of the NO molecule in the vicinity of the $N(1s)^{-1}$ and $O(1s)^{-1}$ ionization thresholds induced by elliptically polarized light.

One of the features distinguishing inner-shell photoionization (PI), when compared to valence-shell photoionization, is that the ionic molecular state produced after the photoelectron ejection further decays by Auger electron emission leading to double, triple, or multiple ionization of the target, as well as dissociation. In this paper we focus on DPI reactions producing a photoelectron, an Auger electron, and two ionic fragments,

$$\begin{aligned} NO(^2\Pi) + h\nu(\hat{\mathbf{e}}) &\rightarrow NO^+\{^3\Pi \text{ or } {}^1\Pi, [N(O)1s]^{-1}\} + e_{ph} \\ &\rightarrow NO^{2+} + e_{ph} + e_{Au} \\ &\rightarrow N^+ + O^+ + e_{ph} + e_{Au}. \end{aligned} \quad (1)$$

Here, the vector correlation method consists of measuring the nascent velocity vectors of the two ionic fragments and the photoelectron e_{ph} collected in a 4π solid angle [5], leading to the $(\mathbf{V_N}, \mathbf{V_O}, \mathbf{V}_e, \hat{\mathbf{e}})$ quadruplet, where $\hat{\mathbf{e}}$ stands for $\mathbf{k}$, the propagation axis of elliptically polarized light, or $\mathbf{P}$, the polarization axis of linearly polarized light. The analysis of the spatial correlations among the $(\mathbf{V_N}, \mathbf{V_O}, \mathbf{V}_e, \hat{\mathbf{e}})$ vectors provides, in particular, the $I(\theta_e, \phi_e, \chi)$ MFPADs, where the polar angle χ characterizes the emission velocity of the ionic fragment $\mathbf{V_A}$ linked to the orientation of the molecular axis with respect to the polarization of the light, and (θ_e, ϕ_e) the $\mathbf{V}_e$ electron emission velocity in the molecular frame, an observable which is the most sensitive probe for the molecular photoionization dynamics [6]. The general expression of $I(\theta_e, \phi_e, \chi)$ has the great advantage of disentangling the information about the photoionization dynamics by expressing the MFPADs for any chosen orientation of the molecular axis with respect to the light axis in terms of only five one-dimensional $F_{LN}(\theta_e)$ functions, where the dependence on ϕ_e and χ is through low-order analytical functions [4].

In this experiment, we note that photoionization followed by single Auger electron emission also leads to the production of the weaker $(N^{2+}+O+e_{ph}+e_{Au})$ and $(N+O^{2+}+e_{ph}+e_{Au})$ DPI channels. Although the Auger decay involves higher NO^{2+} excited states than those participating into reaction (1), as discussed in Sec. IV, these events contain the

*Present address: HASYLAB at DESY, Notkestr. 85, D-22607 Hamburg, Germany

same angular information as the (N^+, O^+, e_{ph}) events reported in this paper.

In order to measure the $(\mathbf{V}_N, \mathbf{V}_O, \mathbf{V}_e, \hat{\mathbf{e}})$ vector correlation, we have used the three-dimensional electron and ion velocity spectrometer developed earlier [5], but now the multihit possibility of the position sensitive detectors and dedicated electronics has been fully exploited to record and analyze the (N^{p+}, O^{q+}, e_{ph}) coincident events (where $p, q = 1, 2\ldots$). For each particle collected in a 4π solid angle, the three components of the velocity vectors are derived from the arrival time and impact position on the detector. Specific conditions arise from the fact that, in the case of inner-shell ionization, the ion fragments are produced with higher kinetic energy than in valence-shell ionization as discussed in Sec. IV. Combined with the BESSY third generation synchrotron light source providing well-resolved temporal structure in the single bunch mode, the vector correlation method enabled us to analyze with both satisfactory energy and angular resolution photoionization events producing photoelectrons and photoions up to about 15 eV kinetic energy. We also took advantage of the delivery of elliptically polarized light to perform complete PI experiments leading to the magnitude and relative phases of the complex dipole matrix elements. A similar level of information has been reported in other experiments, e.g., for the inner-shell ionization of CO and N_2 using the cold-target recoil-ion momentum spectroscopy (COLTRIMS) [7] or angle-resolved photoelectron-photoion coincidence (AR PEPICO) [8] techniques, or valence-shell ionization of NO [4,9].

K-shell photoionization of the open shell NO molecule leading to the $(2\sigma)(2\pi)$ $^3\Pi$ and $^1\Pi$ NO^+ ionic states has been taken as an example to discuss the role of exchange interactions in the description of the shape resonance above the $N(1s)^{-1}$ ionization threshold [10–14]. The two multiplet components are separated by 1.41 eV for $N(1s)^{-1}$ ionization (with ionization potentials I_P of 410.31 and 411.81 eV for $NO^+(^3\Pi)$ and $NO^+(^1\Pi)$, respectively), and 0.48 eV for $O(1s)^{-1}$ ionization (I_P=543.32 eV and 543.83 eV for $^3\Pi$ and $^1\Pi$) [14,15]. In order to investigate the shape resonant dynamics, multiplet-specific $N(1s)^{-1}$ photoelectron angular distributions were first recorded for fixed-in-space molecules parallel to linearly polarized light [13] using the AR PEPICO technique, where a photoelectron analyzer is rotated around the photon beam while ions are detected from a direction fixed in space and parallel to the polarization axis. These data provided a first insight of the dynamics of the σ^* shape resonance in the channels leading to the $^3\Pi$ or $^1\Pi(2\sigma)^{-1}$ NO^+ ionic states: they showed that the odd-parity $f\sigma$ and $p\sigma$ partial waves give dominant contributions to the cross section of both channels in the region of the resonance located at about 415 eV, with a stronger contribution of the $p\sigma$ partial wave in the $^1\Pi$ channel. The multichannel Schwinger configuration interaction (MCSCI) calculations discussed in that paper were consistent with this result for the $^3\Pi$ channel, but differ for the $^1\Pi$ channel. The role of doubly excited states lying above the $N(1s)^{-1}$ ionization threshold and autoionizing into the NO^+ continuum studied, e.g., by O^- anion yield spectroscopy [16] is also invoked in the interpretation of the photoemission data [13]. More recently, Hosaka *et al.* [17] reported multiplet-specific $N(1s)^{-1}$ photoelectron angular distributions for fixed-in-space molecules parallel and perpendicular to linearly polarized light at a photon energy of 416.8 eV using a coincidence velocity imaging apparatus, where two-dimensional velocity map imaging of photoelectrons is carried out, while the three-dimensional velocity vectors of fragment ions are measured. The extraction of the MFPADs for the two geometries required an extension of the peeling method. Finally, in a recent electron-ion-ion coincidence momentum imaging study of the $N(1s)^{-1}$ PI of NO induced by linearly polarized photons with energy of 412 eV [18] the MFPADs for ionization into $NO^+(^3\Pi)$ were analyzed in terms of four one-dimensional functions, following a formalism similar to the one developed in Ref. [3].

In this paper we report on the results of the $(\mathbf{V}_N, \mathbf{V}_O, \mathbf{V}_e, \hat{\mathbf{e}})$ vector correlation analysis for PI of NO induced by elliptically polarized light at the three photon energies $h\nu \approx 413.9$, 415.8, and 418.3 eV in the region of the $2\sigma \rightarrow \sigma^*$ shape resonance above the $N(1s)^{-1}$ ionization threshold, and for $h\nu \approx 550.5$ eV in the region of the $1\sigma \rightarrow \sigma^*$ shape resonance above the $O(1s)^{-1}$ ionization threshold. Brief descriptions of the experimental method and data extraction, and of the MCSCI calculations, are reported in Secs. II and III, respectively. The experimental results are discussed in terms of electron-ion kinetic energy correlation in Sec. IV. In Sec. V we present briefly the theory of measurement for the analysis of molecular frame photoemission induced by elliptically polarized light, and we report the MFPADs both in terms of the complete set of one-dimensional $F_{LN}(\theta_e)$ functions, which determine the generalized MFPAD $I(\theta_e, \phi_e, \chi)$, and in terms of the $I_\chi(\theta_e, \phi_e)$ MFPADs for any orientation χ of the molecule with respect to the quantization axis of the light. In the present experiment the $^1\Pi$ and $^3\Pi$ states were not well resolved in the $(2\sigma)^{-1}$ or $(1\sigma)^{-1}$ channels, therefore we report the MFPADs for Eq. (1) for the sum of the two states at each photon energy. The measured MFPADs are compared with the predictions of corresponding MCSCI calculations for the sum of the two final states, whereas the computed dipole matrix elements are reported separately for each case. The results obtained are discussed in terms of the dependence of the MFPADs upon the photoelectron energy along the $N(1s)^{-1}$ shape resonance, and the comparison of $N(1s)^{-1}$ and $O(1s)^{-1}$ photoemission for a similar photoelectron energy. We note that we have reported partial results for $N(1s)^{-1}$ and $O(1s)^{-1}$ photoemission recently [19].

II. EXPERIMENT: THE VECTOR CORRELATION METHOD

A. Experimental setup

In the double velocity spectrometer described in detail earlier [5], the interaction region is defined at the intersection of a supersonic molecular beam [20] and the BESSY polarized synchrotron radiation on beamline UE 56 PGM1 [21], operated in the single bunch mode (period 800 ns, pulse time width 50 ps), which allows for ion and electron time-of-flight-resolved coincidence detection. Ions and electrons are

extracted from the interaction region by a dc electric field **E** whose magnitude ensures a 4π collection of both particles, and guided to the two delay-line position sensitive detectors (PSDs) (DLD40 Roentdek [22]) through an intermediate region where focusing lens sets are used to control the trajectories [5]. For each (N^+,O^+,e_{ph}) coincident event the three components of the $\mathbf{V_N},\mathbf{V_O}$ ion fragments and $\mathbf{V_e}$ photoelectron nascent velocity vectors are deduced from the time of flight (TOF) and impact position of the particles on their respective PSD. The signal detected on the front MCP of the electron detector is used as a common start for an eight independent channel time-to-digital converter (CTN-TDC [23], encoding resolution 250 ps) with a large multihit capability per channel, and a time-to-amplitude converter (TAC). The TAC is stopped by the electronic signal synchronous with the BESSY light pulse, providing the electron time of flight (TOF_{elec}) with a coding resolution of 25 ps on the 100 ns scale. Four channels of the CTN-TDC are dedicated to the time signals from the ends of the two delay lines of the electron detector leading to the electron position, and the four others to those of the ion detector providing the ion position and time of flight (TOF_{ion}) as described previously [5]. Typical values of TOF_{elec} and TOF_{ion} are in the range of 10–20 ns and a few μs, respectively. Within the dynamical range of the TDC, chosen to be 8 or 16 μs in these measurements, all the "complete" events corresponding to four delay-line signals for each particle and the TAC signal, and containing at least one electron and one ion, were stored (with a maximum of 16 particles). Here we consider the events of the type (one electron, two ions). The finite dead time of about 50 ns of the delay-line detectors and read-out electronics prevents the detection of two electrons arising from a single DPI event, and depending on the ion fragment mass and energy, and the magnitude of the extraction field, it may induce a loss in the ion collection.

The extraction field of 150 V/cm used for the two measurements at $h\nu \approx 418.3$ and 550.5 eV (or 100 V/cm at $h\nu \approx 413.9$ and 415.8 eV) combined with the focusing lenses ensured a 4π collection of singly charged ions and electrons of kinetic energy up to 12 eV (or 8 eV, respectively). The ion fragment kinetic energy limit of 12 eV (8 eV) corresponds for the NO molecule to 22.5 eV (15 eV) of the ion fragment kinetic energy release (KER), i.e., the sum of the kinetic energy of the two fragments. For higher kinetic energy fragments the spatial discrimination gradually reduces the angular collection.

We describe the polarization of the light in terms of the four-component (s_0,s_1,s_2,s_3) Stokes vector that determines the total intensity (s_0), the linear intensity (s_1,s_2), and the circularly polarized intensity (s_3). $(s_1^2+s_2^2+s_3^2)^{1/2}$ and $s_4=s_0-(s_1^2+s_2^2+s_3^2)^{1/2}$ represent the intensity of the components of polarized and unpolarized light, respectively, and the degree of polarization P is accordingly defined as $P=(s_1^2+s_2^2+s_3^2)^{1/2}/s_0$.

B. Selection of events

Figure 1 displays the bidimensional histogram of the (N^{p+},O^{q+},e) events (where $p,q=1$ or 2) distributed as a function of the two ion TOFs, which enables us to identify several structures and select different processes accordingly, recorded at a photon excitation energy $h\nu=413.9$ eV. The (N^+,O^+) events leading to the dominant contribution lie along a diagonal $TOF_{N+}+TOF_{O+} \approx$ constant to a first approximation. This reflects conservation of momentum in the fragmentation process, in the assumption generally valid that the initial momentum of the NO^{2+} molecular ion due to the translation velocity in the molecular beam, or to the ionization process, is negligible compared to the recoil momenta of the energetic N^+ and O^+ ionic fragments. Double Auger decay giving rise to triple ionization of the molecule leads to the production of (N^{2+},O^+,e) or (N^+,O^{2+},e) events, where the slow electron detected in coincidence with the two ion fragments is now either the photoelectron or an Auger electron. In Fig. 1, the (N^{2+},O^+) or (N^+,O^{2+}) events lie roughly along a straight line characterized by a slope −2. The analysis of those events involving the photoelectron provides the same angular information about the PI reaction as that achieved in the analysis of the (N^+,O^+,e_{ph}) events. The data involving detection of a slow Auger electron will be discussed in another publication.

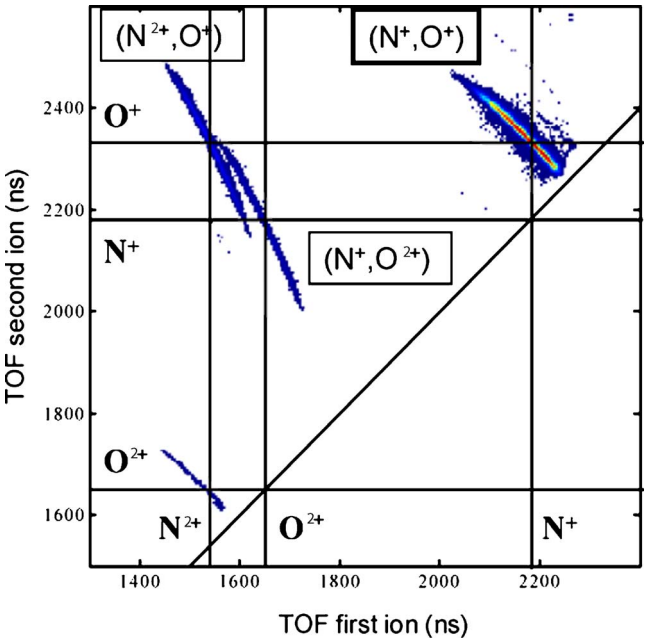

FIG. 1. (Color online) TOF-TOF bidimensional histogram of the (N^{p+},O^{q+},e) events (where p, $q=1$ or 2) for PI of NO at $h\nu=413.9$ eV. (N^+,O^+) events lie along a diagonal $TOF_{N+}+TOF_{O+} \approx$ constant of slope −1 and the (N^{2+},O^+) or (N^+,O^{2+}) events lie along a straight line of slope −2.

With the extraction field of 150 V/cm, the TOF_{N+} and TOF_{O+} distributions partially overlap, therefore a certain amount of (N^+,O^+) coincident events are lost due to the finite dead time of the delay-line detectors and read-out electronics. In order to obtain a complete angular distribution of the molecular axis, we restrict the analysis to the (N^+,O^+,e) events corresponding to N^+ fragments emitted in the direction of the ion PSD in a 2π emission solid angle, which we refer to as the forward (FW) N^+ ion fragments: the FW TOF_{N+} region does not overlap with the TOF_{O+} distribution.

Even when restricted from a 4π to a 2π N^+ angular collection, keeping a 4π angular acceptance of the electrons, the $I(\theta_e, \phi_e, \chi)$ molecular frame photoelectron angular distribution is physically complete, since all the possible angular correlations (molecular orientation with respect to the light polarization axis, and photoelectron with respect to the molecular axis) are equally represented.

The data analysis providing the (V_x, V_y, V_z) velocity components from the positions and TOFs for each particle of one (N^+, O^+, e) event in the presence of focusing lenses is similar to the procedure described earlier [5]. Even if the focusing lenses reduce significantly the broadening effects due to the finite dimensions of the interaction region, an additional correction may be applied to further improve the spatial resolution: since both ion fragments are detected, conservation of momentum in the process $NO^{2+} \rightarrow N^+ + O^+$ can be used this time along the x and y axes, in the same assumption as discussed above, to correct the events for the remaining spatial extension of the target. The x_{ion} and y_{ion} correction histograms are also used as a filter to reject noisy events, and to some extent to discriminate the events produced in the supersonic expansion from those arising from the minor thermalized component. Finally, the position of the electron along the y axis parallel to the light propagation axis is corrected event by event [5].

III. THEORY SECTION

A. MCSCI method

In order to understand the features found in the observed MFPADs, theoretical calculations of NO K-shell photoionization have been performed using the MCSCI method [24–26]. This method relies on a very accurate approximation of both initial and ion states involved in the photoionization process, obtained using configuration interaction wave functions built on a basis set of optimized orbitals. The photoionization amplitudes are then computed within a variational Schwinger procedure that includes the main interacting channels participating in the process and it is implemented expanding the electronic wave functions over a set of single-center spherical functions.

A multiconfiguration self-consistent field (MCSCF) calculation of the NO^+ ground state has been performed first at the experimental NO ground state equilibrium bond distance of 1.150 77 Å [27] using all core and valence orbitals expanded over Dunning's aug-cc-pVTZ basis set [28]. The resulting set of six σ and two π natural orbitals has then been used as the basis set for a full CI representation of the $NO(^2\Pi)$ ground state and $NO^+(^3\Pi, ^1\Pi)$ states corresponding to $N(1s)^{-1}$ and $O(1s)^{-1}$ ionization thresholds. In order to achieve an accurate representation of the $1s$ orbitals, the single-center expansion included spherical functions with l up to 120 for the bound and continuum orbitals, while only a maximum l of 18 was used to describe the photoelectron in the asymptotic region. Within this approximation, the computed ionization potentials are 411.69 eV ($^3\Pi$) and 412.54 eV ($^1\Pi$) for $N(1s)^{-1}$ and 543.33 eV ($^3\Pi$) and 543.92 eV ($^1\Pi$) for $O(1s)^{-1}$ photoionization. The last values compare very well with the corresponding experimental ones, 543.3 eV ($^3\Pi$) and 543.8 eV ($^1\Pi$), respectively, whereas present calculations seem to slightly overestimate the ionization potentials for the $N(1s)^{-1}$ channels, which have been found experimentally at 410.3 eV ($^3\Pi$) and 411.8 eV ($^1\Pi$).

For a better comparison with the measured data, the experimental ionization potentials have been used in the final two-channels MCSCI calculations for all the photoionization processes considered here. This may affect the interaction between the two channels bringing a slightly different picture of the photoionization dynamics than the one reported in earlier studies [13,14].

B. Cross sections and asymmetry parameters

The $N(1s)^{-1}$ photoionization has been earlier investigated theoretically [11] and a shape resonance just above threshold has been found to be responsible for the main behavior of both $N(1s)^{-1}$ $^3\Pi$ and $^1\Pi$ channels. Here we have carried out initial MCSCI calculations with a reduced set of single-center functions (l up to 60) to inspect the dynamics of both $N(1s)^{-1}$ and $O(1s)^{-1}$ core photoionization processes over an extended range of photon energy. This preliminary study was very helpful in understanding the effect of the shape resonances on the MFPADs measured at photon energies in close proximity to the resonance peaks. Figure 2 shows the total photoionization cross section along with the β_N and β_e asymmetry parameters for $N(1s)^{-1}$ (left panel) and $O(1s)^{-1}$ (right panel) processes.

The $N(1s)^{-1}$ photoionization is examined with more detail in Fig. 3, where the theoretical results are summarized for $^3\Pi$ and $^1\Pi$ channels and compared with the available experimental data [14]. The predicted $^3\Pi/^1\Pi$ ratio [Fig. 3 (bottom)] deviates from the experimental values at low energies since the maximum of the σ^* shape resonance does not occur at the same energy in both channels. The nuclear and electronic asymmetry parameters for each channel are reported in Fig. 4; they display a similar evolution with the photon excitation energy.

The MFPADs computed with the full set of spherical functions ($l=120$) for selected photon excitation energies are presented in Secs. V B and V C and compared with the present measurements of the sum of the two final states, for $N(1s)^{-1}$ and $O(1s)^{-1}$ photoionization of NO. The analysis of the $O(1s)^{-1}$ photoionization is performed for the first time. Both continua are affected by shape resonances and the dynamics of the emitted photoelectron is studied in terms of partial waves contributions. The dipole matrix elements for the $^3\Pi$ and $^1\Pi$ state selected photoionizations are reported in Sec. V D.

IV. ION-ELECTRON KINETIC ENERGY CORRELATION

Figure 5(a) displays the ion-electron kinetic energy correlation diagram (KECD) for the $(N^+, O^+, e_{\text{ph}})$ events at the photon excitation energy $h\nu=415.8$ eV, a few eV above the $N(1s)^{-1}$ ionization threshold, i.e., the occurrence of the $(N^+, O^+, e_{\text{ph}})$ events as a function of the ion fragment kinetic energy release (KER) and the electron energy (E_e). For all

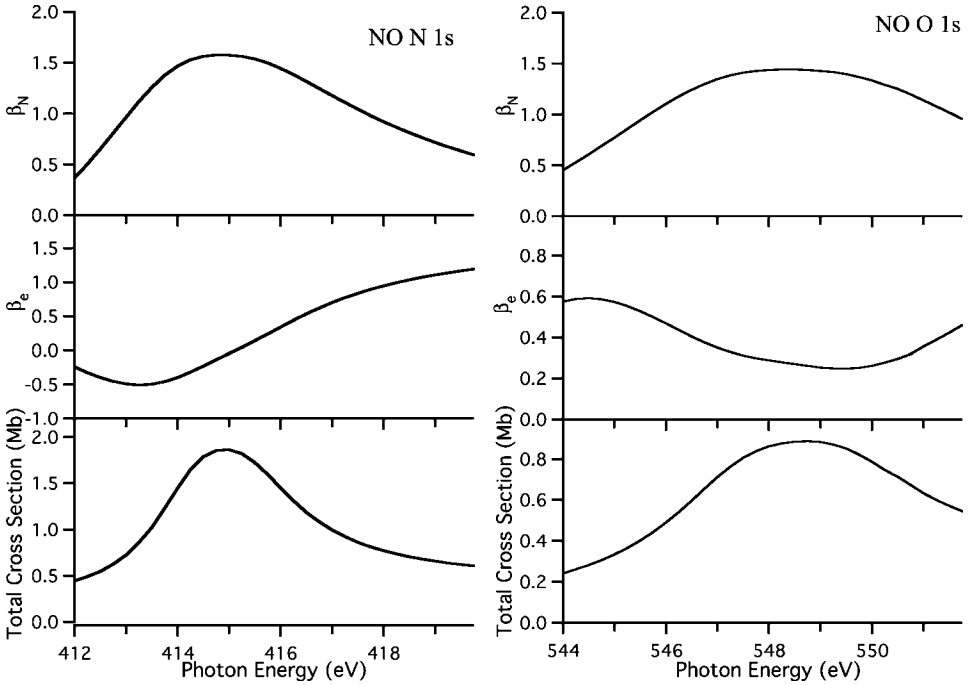

FIG. 2. Computed $NO^+(^3\Pi, ^1\Pi)$ total photoionization cross section, along with the β_N and β_e asymmetry parameters for $N(1s)^{-1}$ (left panel) and $O(1s)^{-1}$ (right panel) ionization processes.

the events displayed the angular collection is complete (2π and 4π angular acceptance for ions and electrons, respectively). The structures identified in the KECD show that the dominant channel corresponds to ionization into the $NO^+(^3\Pi)$ substate and a KER of about 9.5 eV at the maximum. Ionization into the $NO^+(^3\Pi)$ and $NO^+(^1\Pi)$ multiplets is partially resolved, and the KER distribution is very comparable for the two substates.

The one-dimensional (1D) photoelectron and KER energy spectra shown on the left and top sides of the KECD [Figs. 5(b) and 5(c)] correspond to the projections of the 2D histogram onto the E_e and KER axes, respectively. The photoelec-

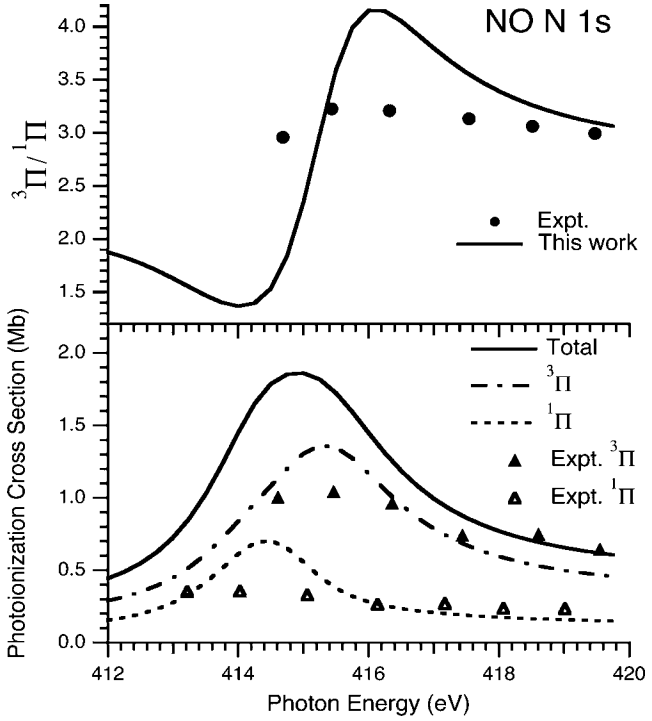

FIG. 3. Theoretical $NO^+(^3\Pi)$ and $(^1\Pi)$ partial photoionization cross sections above the $N(1s)^{-1}$ threshold (bottom) and $^3\Pi/^1\Pi$ ratio (top) compared with the experimental data from Rüdel *et al.* [14].

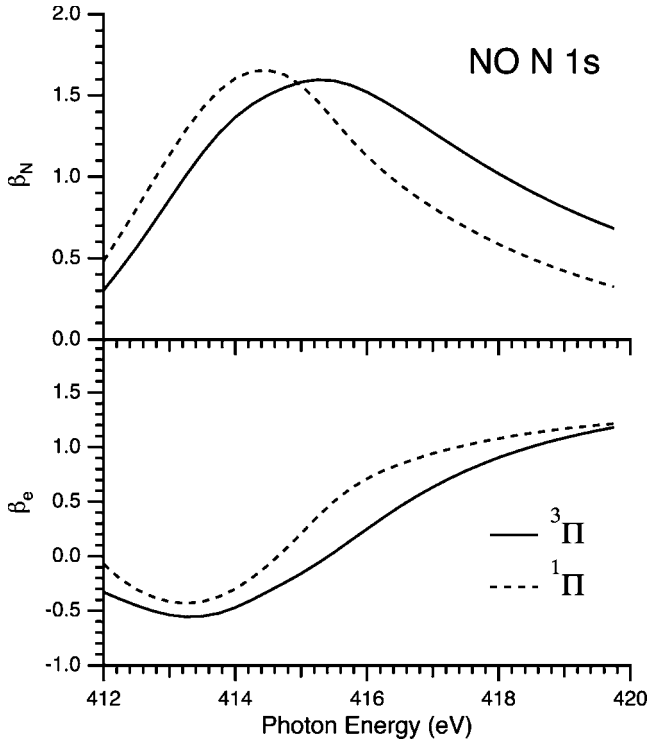

FIG. 4. Computed β_N nuclear and β_e electronic asymmetry parameters for the $(2\sigma)^{-1}$ $NO^+(^3\Pi)$ and $(^1\Pi)$ channels.

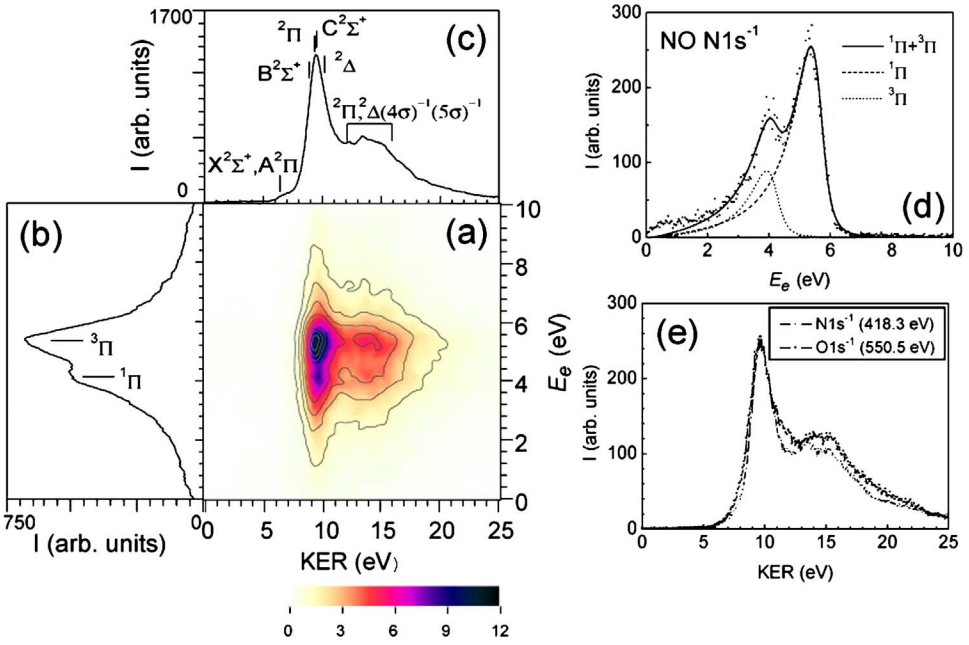

FIG. 5. (Color online) (a) (KER, E_e) KECD for the (N^+,O^+,e_{ph}) events at $h\nu$=415.8 eV in the $0 \leqslant$ KER $\leqslant 25$ eV and $0 \leqslant E_e \leqslant 10$ eV energy window (complete angular collection). The extraction field E_{ext}=100 V/cm is combined with Λ_e and Λ_{A+} standard focusing lens sets. The intensity scale runs from white (lowest intensity) to black (highest intensity) in a linear scale as shown; the contour lines are spaced by 10% of the maximum value. (b) 1D photoelectron spectrum. (c) KER energy spectrum. (d) Photoelectron spectrum for the selection of events with $80° \leqslant \alpha_{el,z} \leqslant 100°$ (see the text). (e) Comparison of the KER spectra for the (N^+,O^+,e_{ph}) events at $h\nu$=550.5 eV, and $h\nu$=418.3 eV for the same extraction field of 150 V/cm.

tron spectrum displayed in the inset of Fig. 5(d) corresponds to a specific selection of events characterized by a better energy resolution than that of all events seen in the projection (b). In Fig. 5(d) we select those events for which the electron emission polar angle with respect to the spectrometer's z axis is in the interval $80° \leqslant \alpha_{el\text{-}z} \leqslant 100°$, such that the $V_{z,el}$ component gives a small contribution to the energy, which is then mainly determined by the $V_{x,el}$ and $V_{y,el}$ components parallel to the PSD. This angular selection has been controlled to preserve the cross-section ratio. Fitting the electron energy spectrum to a model profile that takes into account postcollisional interaction (PCI) effects [29] leads to an estimation of the cross-section ratio between ionization into the $NO^+(^3\Pi)$ and $NO^+(^1\Pi)$ ionic states of the order of 3.1, close to the statistical ratio 3:1 and consistent with previous measurements [12,14].

The vector correlation method as used in the present context for K-shell ionization does not provide an unambiguous determination of the populated NO^{2+} molecular ionic states and $(N^+ + O^+)$ dissociation limits, since the Auger electron taking part in the reaction is not included in the analyzed (N^+,O^+,e_{ph}) events. However, the measured KER distribution, combined with spectroscopic studies of the NO^{2+} molecular dication by different techniques (see, e.g., Ref. [30] and references therein) enable us to propose to some extent an assignment of the NO^{2+} electronic states populated after Auger decay, and their dissociation limits. Dissociation pathways from the $N(1s)^{-1}$ and $O(1s)^{-1}$ core-hole states were suggested previously from the broad kinetic energy distribution of the ionic fragments measured by TOF spectrometry [31]. The KER spectrum in Fig. 5(c) displays three structures: a weak bump in the 6–8 eV interval, a dominant, well-defined peak ranging from 8.5–11 eV with a maximum at 9.5 eV, and a broad peak extending from 11.5–20 eV, with a flat maximum in the 11.5–15 eV KER range. Three comparable KER regions were identified with a broader energy resolution for 80–100 eV photon excitation energies using the PIPICO technique [32]. It is noticeable that the KER distribution does not involve larger values than those at 100 eV for the presently recorded 413–419 and 550 eV photon energies. The $(N^+ - O^+)$ KER distributions have also been studied in electron impact ionization using Doppler-free kinetic energy release spectroscopy [33]. Combined with the results of x-ray Auger electron spectroscopy [34,35], which can be used to identify the population of NO^{2+} ionic states in several energy regions, and *ab initio* calculations of potential energy curves of the dication [33–37], the measured KER distributions are consistent with the following assignments:

(i) The weak low KER peak corresponds to the dissociative component of Auger decay into the lowest NO^{2+} ($X\,^2\Sigma^+$ and $A\,^2\Pi$) ionic states involving the $\{N^+(^3P)+O^+(^4S)\}$ ground state dissociation limit with a KER threshold at 6.3 eV [32].

(ii) The dominant peak at the maximum can be attributed to the population of selected ionic states of $^2\Sigma^+$, $^2\Pi$, and $^2\Delta$ symmetries lying at about 49 eV above the $NO(^2\Pi)$ ground state in the Franck-Condon (FC) region, which correspond to the $[(5\sigma)^1(1\pi)^3(2\pi)^1]$, $[(5\sigma)^0(1\pi)^4(2\pi)^1]$, and $[(5\sigma)^2(1\pi)^2(2\pi)^1]$ leading electronic configurations [two electrons ejected from the (5σ) and/or (1π) MOs]. In the

TABLE I. Selection of dissociation limits relevant for Fig. 5(c). The energy positions of the dissociation limits (E_D) and NO^{2+} states are referred to the NO (X, $\nu=0$) origin. Estimated KERs corresponding to the fragmentation schemes of a NO^{2+} ionic state located about 49 eV (I), 53.5 eV (II), 56.5 eV (III), and 60.5 eV (IV) (see text) in the FC region. All energies are given in units of eV.

Dissociation limit	E_D	KER (I)	KER (II)	KER (III)	KER (IV)
$N^+(^3P)+O^+(^4S)$	34.65	14.35	18.85	21.85	
$N^+(^1D)+O^+(^4S)$	36.55	12.45	16.95	19.95	
$N^+(^3P)+O^+(^2D)$	37.97	11.03	15.53	18.53	
$N^+(^1S)+O^+(^4S)$	38.7	10.3	14.8	17.8	
$N^+(^3P)+O^+(^2P)$	39.66	9.34	13.84	16.84	
$N^+(^1D)+O^+(^2D)$	39.86	9.14	13.64	16.64	
$N^+(^1D)+O^+(^2P)$	41.56	7.44	11.94	14.94	
$N^+(^1S)+O^+(^2D)$	42.02	6.98	11.48	14.48	
$N^+(^1S)+O^+(^2P)$	43.71	5.29	9.79	12.79	
$N^{2+}(^2P)+O(^3P)$	50.64			6	10
$N^{2+}(^2P)+O(^1D)$	52.61				
$N^{2+}(^2P)+O(^1S)$	54.83				
$N(^4S)+O^{2+}(^3P)$	55.25				

calculations the $^2\Pi$ and $^2\Delta$ symmetries are predicted to yield the higher intensities in the KLL Auger spectrum [34–36]. The maximum of the KER peak may be assigned to the most probable dissociation limits: $\{N^+(^3P)+O^+(^2P)\}$ and/or $\{N^+(^1S)+O^+(^4S)\}$ (Table I). Ionization into the NO^{2+} ($B\ ^2\Sigma^+[(4\sigma)^1(5\sigma)^2(1\pi)^4]$) state lying at 43.3 eV in the FC region, and leading to the ground state dissociation limit, might also contribute to this peak.

(iii) Finally, the broad structure corresponding to the larger KERs (11.5–20 eV) can be assigned to Auger decay involving $^2\Pi$ and $^2\Delta$ NO^{2+} ionic states of dominant $(4\sigma)^{-1}(5\sigma)^{-1}$ electronic configurations, lying within the FC region at about 53–54 eV and 56–57 eV above $NO(X,v=0)$ in Auger electron spectra and *ab initio* calculations [34–36]. The continuous shape of this structure is consistent with the repulsive character of the NO^{2+} potential energy curves in this region, and the excitation of several dissociation limits as suggested in Table I.

Analysis of the (N^{2+},O,e_{ph}) and (N,O^{2+},e_{ph}) events provides complementary information about the NO^{2+} ionic states populated after Auger decay. The KER spectrum corresponding, e.g., to the (N^{2+},O,e_{ph}) events (PI followed by single electron Auger decay) is obtained by the appropriate weighted subtraction of the (N^{2+},e_{ph}) and (N^{2+},O^+,e_{ph}) events, since PI followed by double electron Auger decay—where the O^+ partner ion is not detected due to the limited efficiency of the ion detector—contributes to the (N^{2+},e_{ph}) signal. It represents about 10% of the (N^+,O^+,e_{ph}) events, taking into account the global efficiencies. The resulting KER distribution has its maximum at about 10 eV, which corresponds to NO^{2+} ionic states lying more than 60 eV above the $NO(^2\Pi)$ ground state and may be assigned to $(4\sigma)^{-2}$ or higher inner-shell excited electronic configurations.

Very comparable results have been obtained at the other energies studied, which are not reported here. We only display in Fig. 5(e) the KER spectrum obtained in the analysis of the (N^+,O^+,e_{ph}) events at $h\nu=550.5$ eV, above the $O(1s)^{-1}$ ionization threshold, compared with the one obtained at $h\nu=418.3$ eV above the $N(1s)^{-1}$ ionization threshold, for the same extraction field of 150 V/cm. The two distributions display similar characteristics, consistent with the very comparable $N(1s)^{-1}$ and $O(1s)^{-1}$ Auger spectra [34]. The small differences in the energy position of the peaks may be attributed to different FC regions for the Auger transitions for the two core-hole states as discussed in Ref. [34].

In the next section we report the angular analysis for the DPI processes after energy selection in the KECD. As mentioned in the Introduction, the complete angular analysis is presented for the sum of the two reactions: PI into the $NO^+(^3\Pi)$ and $NO^+(^1\Pi)$ ionic states. Since the cross-section ratio is of the order of 3:1, the angular distributions are dominated by the contribution of PI into the $NO^+(^3\Pi)$ triplet state.

V. MOLECULAR FRAME PHOTOEMISSION

A. Theory of measurement, MFPAD observables

The theory of measurement for the photoionization of linear molecules in the framework of the dipole approximation and for a single elliptical polarization of the light is presented in detail in another paper [38]. In the case of elliptically polarized light the general expression of the MFPAD is a function of four angles $I(\theta_e,\phi_e,\chi,\gamma)$ [4] where the polar angle χ and the azimuthal angle γ describe the orientation of the molecule with respect to the light propagation axis $\mathbf{y}$, and (θ_e,ϕ_e) is the emission direction of the photoelectron in the molecular frame defined by the molecular axis $\mathbf{z_{mf}}$ and the light propagation axis. The three-dimensional Legendre (χ) and Fourier (ϕ_e,γ) expansion of this distribution enables one to extract the four $F_{LN}(\theta_e)$ functions $(F_{00},F_{20},F_{21},F_{22})$, the

product of the fifth F_{11} function and the Stokes parameter s_3, and the two Stokes parameters s_1 and s_2. If the degree of polarization of the light P is close to 1, s_3 is determined as well, and the five $F_{LN}(\theta_e)$ functions are obtained. The $F_{LN}(\theta_e)$ functions are expanded in terms of the partial-wave dipole matrix elements for the PI transition, as defined previously for linearly and circularly polarized light [3,4]. Their determination provides the conditions of a complete PI experiment.

We note that, for any s_1 and s_2, the generalized expression for $I(\theta_e, \phi_e, \chi)$ MFPAD, ignoring the γ angular dependence, is

$$\begin{aligned} I(\theta_e,\phi_e,\chi) = {} & F_{00}(\theta_e) - 0.5F_{20}(\theta_e)P_2^0(\cos\chi) \\ & - 0.5F_{21}(\theta_e)P_2^1(\cos\chi)\cos\phi_e \\ & - 0.5F_{22}(\theta_e)P_2^2(\cos\chi)\cos 2\phi_e \\ & - s_3F_{11}(\theta_e)P_1^1(\cos\chi)\sin\phi_e, \end{aligned} \tag{2}$$

and enables us to determine the four $F_{LN}(\theta_e)$ functions $(F_{00}, F_{20}, F_{21}, F_{22})$ if the reference axis is the light propagation axis regardless of the polarization chosen.

In Sec. V B we first present the molecular frame angular results in terms of the five $F_{LN}(\theta_e)$ functions for each reaction studied, namely, here for PI into the $N(1s)^{-1}$ $NO^+(^3\Pi$ and $^1\Pi)$ sum of the multiplet state channels and PI into the $O(1s)^{-1}$ $NO^+(^3\Pi$ and $^1\Pi)$ ones. This presentation enables a detailed comparison of the five measured F_{LN} functions for a given photon excitation energy with the theoretical F_{LN} functions, obtained as the sum of the multiplet specific F_{LN} functions for PI into the $NO^+(^3\Pi)$ and $(^1\Pi)$ ionic states computed for the corresponding photoelectron energies. Since the axial recoil approximation [39] may be reasonably applied to the studied processes (see Sec. V B) the two sets of F_{LN} functions can be directly compared. We note that here θ_e is the electron polar emission angle relative to the NO molecular axis, oriented such that $\theta_e = 0°$ corresponds to an electron emission in the direction of the N end of the molecule ($\mathbf{z_{mf}}$).

Section V B also includes the dimensionless CDAD parameter (circular dichroism for the angular distribution in the molecular frame), which characterizes the effect on the MFPAD of a change from +1 to −1 in the helicity of circularly polarized light. For a molecule oriented perpendicular to the light propagation axis and for electron emission in the half-plane perpendicular to the propagation axis ($\phi_e = 90°$) the CDAD is defined as

$$\mathrm{CDAD}_{(\chi=90,\phi_e=90)} = \frac{I_{+1} - I_{-1}}{I_{+1} + I_{-1}}. \tag{3}$$

This parameter is easily evaluated as [40]

$$\mathrm{CDAD}_{(\chi=90,\phi_e=90)} = \frac{2F_{11}}{2F_{00} + \frac{1}{2}F_{20} + 3F_{22}}. \tag{4}$$

It also characterizes the left-right ($\phi_e = 90°/\phi_e = 270°$) asymmetry of the MF photoemission probability in the plane perpendicular to the propagation axis of circularly polarized light of definite helicity.

The extraction of the dipole matrix elements from the Legendre polynomial expansion of the measured $F_{LN}(\theta_e)$ functions (see, e.g., Ref. [3]) has not been attempted here since the reported $F_{LN}(\theta_e)$ functions correspond to the sum of the $NO^+(^3\Pi$ and $^1\Pi)$ ionization channels. A discussion of the contributions of the dipole matrix elements to each multiplet specific PI reaction based on the MCSCI calculations is presented in Sec. V D.

In Sec. V C we compare the measured and computed $I_\chi(\theta_e, \phi_e)$ MFPADs for the $N(1s)^{-1}$ and $O(1s)^{-1}$ PI processes at similar photoelectron energies with the help of 3D plots, which visualize the dominant partial waves of the continuum electron wave function for chosen molecular orientations. Here we select the MFPADs for a molecule aligned parallel, perpendicular, and at the magic angle with respect to linearly polarized light, as well as the MFPAD for a molecule aligned perpendicular to the propagation axis of circularly polarized light of helicity +1. The intensity distributions are calculated using the $F_{LN}(\theta_e)$ functions according to the following equations [40]:

$$I_{\chi=0}(\theta_e) = F_{00}(\theta_e) + F_{20}(\theta_e),$$

$$I_{\chi=90}(\theta_e,\phi_e) = F_{00}(\theta_e) - 0.5F_{20}(\theta_e) + 3F_{22}(\theta_e)\cos(2\phi_e),$$

$$\begin{aligned} I_{\chi=54.7}(\theta_e,\phi_e) = {} & F_{00}(\theta_e) + 1.41F_{21}(\theta_e)\cos(\phi_e) \\ & + 2F_{22}(\theta_e)\cos(2\phi_e), \end{aligned}$$

$$\begin{aligned} I_{\pm1\chi=90}(\theta_e,\phi_e) = {} & F_{00}(\theta_e) + 0.25F_{20}(\theta_e) \pm F_{11}(\theta_e)\sin(\phi_e) \\ & - 1.5F_{22}(\theta_e)\cos(2\phi_e). \end{aligned} \tag{5}$$

We note that in the description of the MFPADs for molecules tilted with respect to linearly polarized light, the azimuthal angle is defined such that $\phi_e = 0°$ and $\phi_e = 180°$ correspond to the emission of electrons within a plane containing both the molecular and the polarization axes, $\phi_e = 0°$ and $\phi_e = 180°$ characterizing the half planes which contain the N or the O end of the molecule, respectively. Alternatively, in the description of the MFPADs for circularly polarized light, the azimuthal angle is defined such that $\phi_e = 0°$ and $\phi_e = 180°$ correspond to electron emission within a plane that contains both the molecular and the light propagation axes. As mentioned above, for the $I_{\pm1\chi=90}(\theta_e, \phi_e)$ MFPAD of a molecule oriented perpendicular to the propagation axis with the N end pointing in the $\mathbf{z_{mf}}$ direction, $\phi_e = 90°$ and $\phi_e = 270°$ correspond to electron emission in the two half planes perpendicular to the light propagation axis, on the left (right) side when the propagation axis points onto the plane of the figure, respectively. The cuts of these MFPADs for selected ϕ_e azimuthal angles presented in Sec. V C are also informative for a detailed comparison of the measured MFPADs with the calculations.

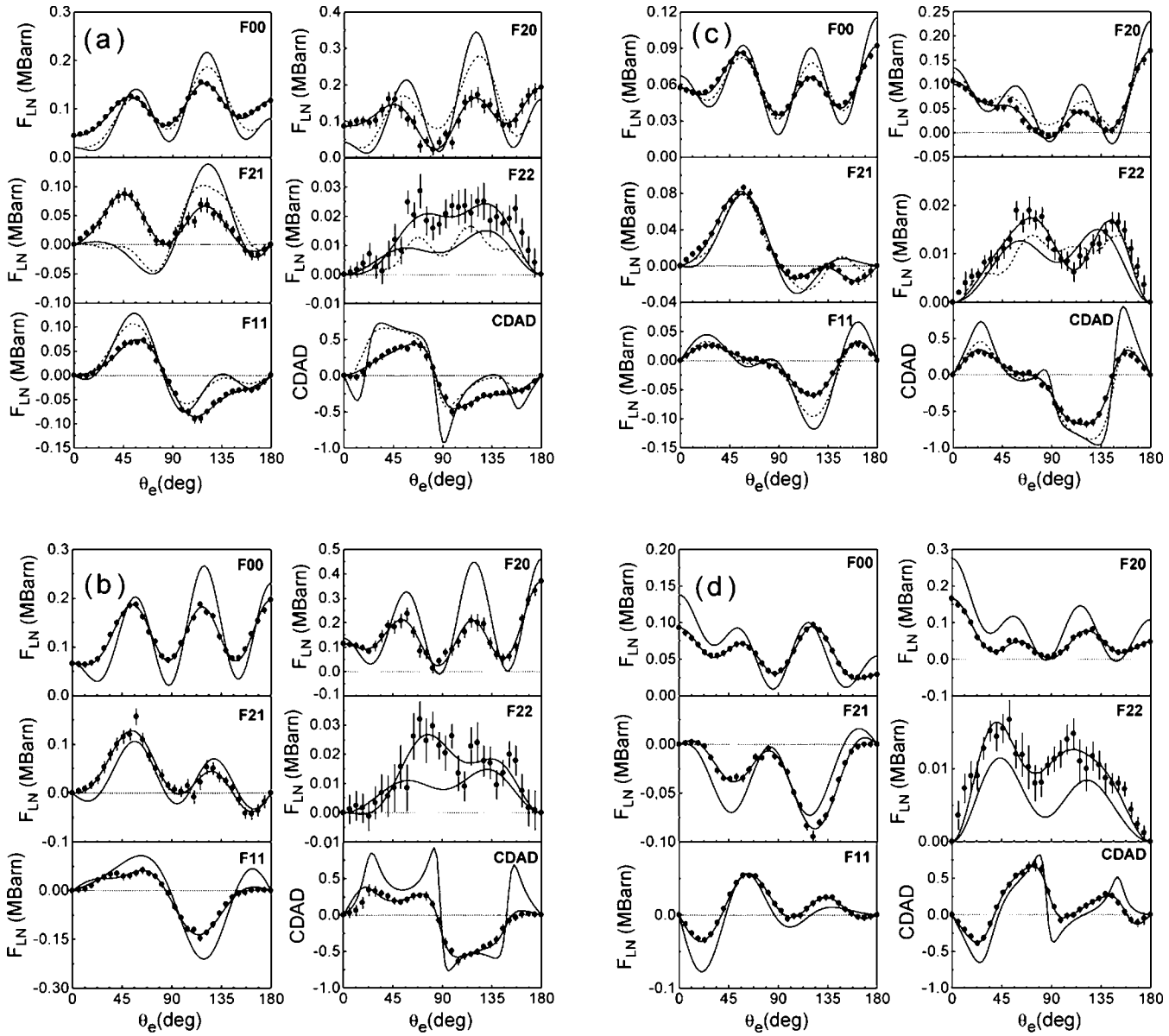

FIG. 6. Measured F_{LN} functions in Mbarn and the CDAD parameter (unitless) (dots) for PI into $NO^+(^3\Pi$ and $^1\Pi)$ $N(1s)^{-1}$ at (a) $h\nu \approx 413.9$ eV, (b) 415.8 eV, and (c) 418.3 eV and (d) $NO^+(^3\Pi$ and $^1\Pi)$ $O(1s)^{-1}$ at $h\nu \approx 550.5$ eV compared with MCSCI calculations (full line). (a) and (c) include the calculations convoluted with the apparatus function using a Monte Carlo simulation (dashed line). The experimental data are normalized such that the total PI cross sections are the same as the computed total cross section. The lines passing through the experimental data are fits of the experimental data using truncated expansions of Legendre polynomials.

B. MFPADS for PI into the $NO^+(^3\Pi$ and $^1\Pi)$ ionization channel: F_{LN} functions

1. Axial recoil approximation

The MFPADs, including the value of the β_{ion} asymmetry parameter that characterizes the symmetry of the molecular state in the continuum, are the fingerprints of a given PI reaction and they do not depend *a priori* on the subsequent dissociation of the molecular ion. The analysis of the vector correlations for all the observed DPI channels corresponding to a complete collection of the $(N^+, O^+, e_{\text{ph}})$ events for the PI of NO leading to $NO^+(^3\Pi, ^1\Pi)$ ionic states yields identical MFPADs within the axial recoil (AR) approximation. However, if the AR approximation breaks down in selected dissociation channels, as previously observed, e.g., for *K*-shell PI of CO [41], the measured recoil frame photoelectron angular distributions (RFPADs) depend on the DPI channels and the original MFPAD may be partially smeared out. A careful analysis of the $F_{LN}(\theta_e)$ functions for such reactions may then provide an estimation of the lifetime of the molecular ion prior to dissociation [42].

A first evaluation of the validity of the AR approximation for the studied reactions is achieved by comparing the measured β_R recoil ion fragment asymmetry parameters, for selected DPI channels identified by their kinetic energy release. When elliptically polarized light is used β_R may be deter-

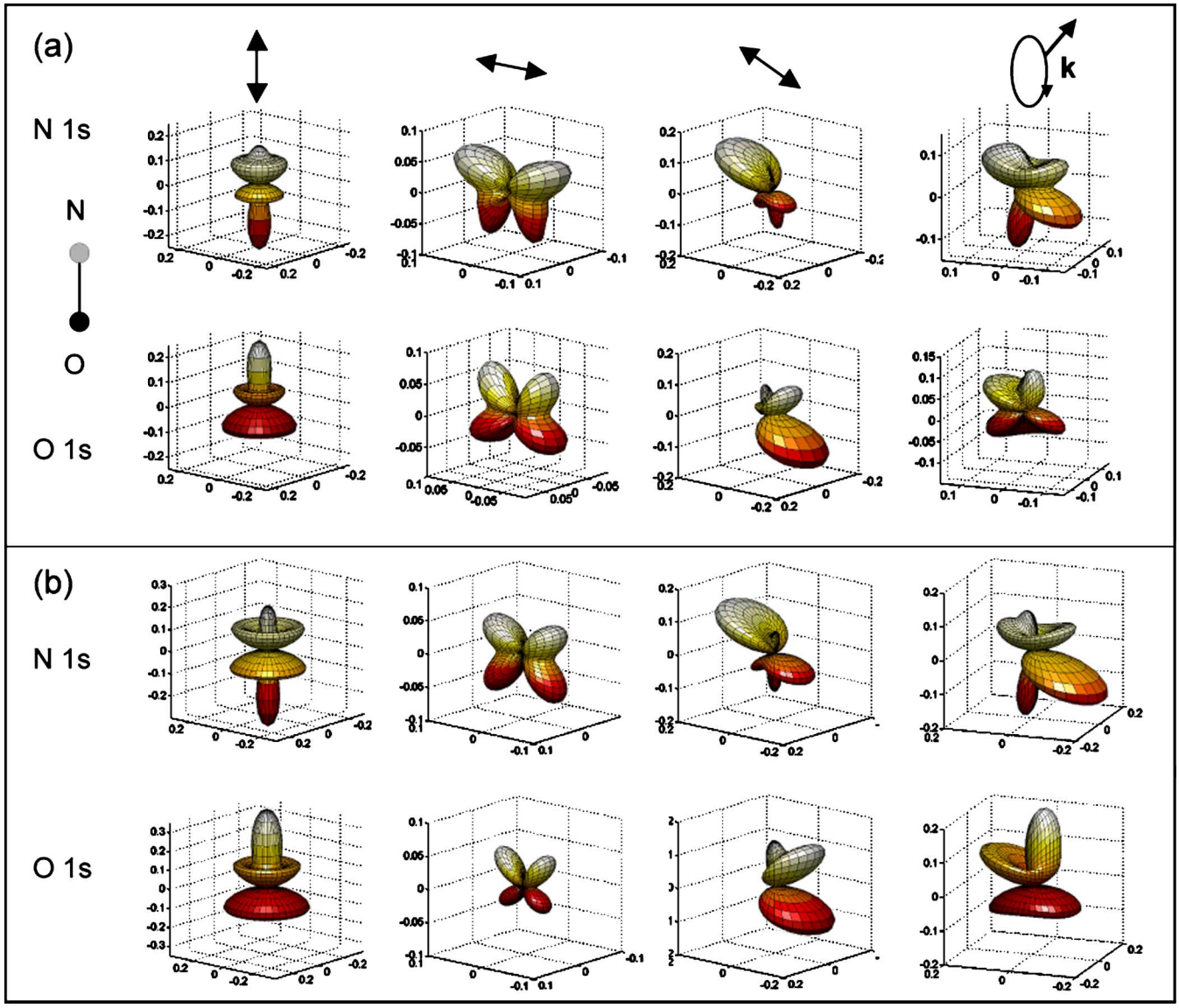

FIG. 7. (Color online) Measured (a) and computed (b) $N(1s)^{-1}$ and $O(1s)^{-1}$ $I_\chi(\theta_e,\phi_e)$ MFPADs at $h\nu$=418.3 eV and 550.5 eV, for a molecule aligned parallel (χ=0°), perpendicular (χ=90°), at the magic angle (χ=54.7°) with respect to linearly polarized light, and for a molecule aligned perpendicular (χ=90°) to the propagation axis of circularly polarized light ($h=+1$). The molecular axis is vertical with the N end on top as shown. Theory and experiment are normalized such that the total PI cross sections for each reaction are identical.

mined by analyzing the laboratory frame photoion polar angle distribution with respect to the light propagation axis, according to the expression

$$I(\chi) = I_0\left\{1 - \frac{\beta_R}{2}P_2(\cos\chi)\right\}. \tag{6}$$

We note that when the complete angular distribution $I(\theta_e,\phi_e,\chi)$ is considered [Eq. (2)], the β_R asymmetry parameter may also be obtained as

$$\beta_R = \frac{\int_0^\pi F_{20}\sin\theta\, d\theta}{\int_0^\pi F_{00}\sin\theta\, d\theta}. \tag{7}$$

For PI of NO [reaction given in Eq. (1)] at a given photon excitation energy, we measure identical values of the β_R asymmetry parameter for the two main KER regions discussed in Sec. IV: the peak ranging from 8.5 to 11 eV, and the broad structure extending from 11.5 to 20 eV where NO^{2+} repulsive states are expected to undergo fast dissociation. This strongly supports the validity of the AR approximation for *K*-shell ionization of NO, as previously found for

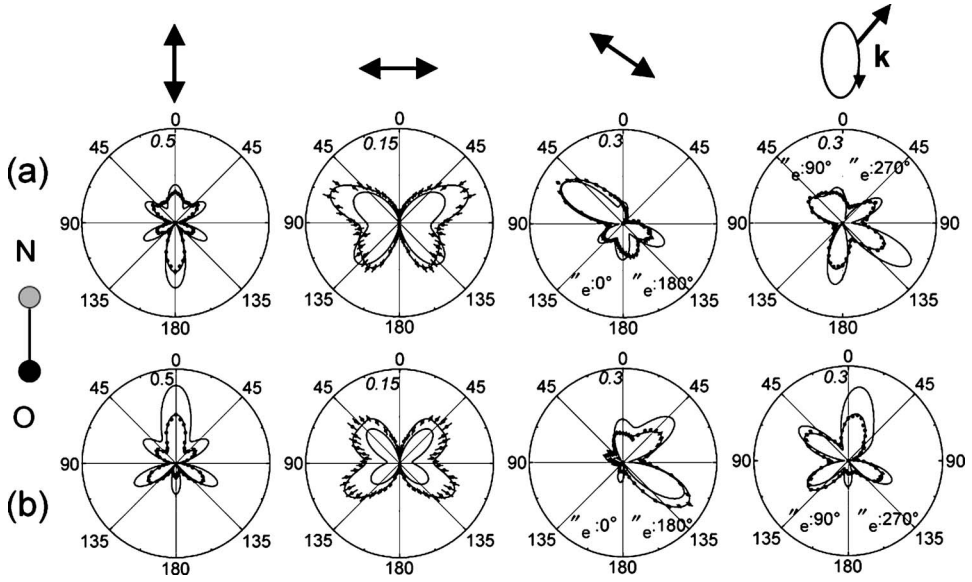

FIG. 8. Cuts of the $N(1s)^{-1}$ (a) and $O(1s)^{-1}$ (b) $I_\chi(\theta_e,\phi_e)$ MFPADs shown in Fig. 7 for selected ϕ_e azimuthal angles: $\phi_e=0°$ for ($\chi=0°$) and ($\chi=90°$), $\phi_e=0°$ and $\phi_e=180°$ for ($\chi=54.7°$), with respect to linearly polarized light, and $\phi_e=90°$ and $\phi_e=270°$ for ($\chi=90°$) with respect to the propagation axis of circularly polarized light ($h=+1$) (see the text). Experimental (dots) and computed (full line) results.

N_2[41], which implies $\beta_R=\beta_{\text{ion}}$. The measured values for β_{ion} at the four studied photon excitation energies are reported in Table II. β_{ion} is close to 1 for the lowest energies, corresponding to a dominant parallel transition in the shape resonance region, and significantly decreases when the photon excitation energy increases. This energy dependence is consistent with a previous study of the anisotropic dissociation of NO [43] above *K*-shell ionization, although the measured β_{ion} values were found to be lower, decreasing from 0.65 at $h\nu=414$ eV to 0.1 at $h\nu=418$ eV and $h\nu=550.5$ eV. We also note that we measure an asymmetry parameter close to $\beta_{\text{ion}}\approx-1$ for the $1s\rightarrow\pi^*$ resonant excitation at $h\nu=399.7$ eV (against −0.75 in Ref. [43]). The energy dependence of the computed β_{ion} parameter is in fair agreement with the experimental one, decreasing from $\beta_{\text{ion}}\approx1.4$ near the maximum of the shape resonance to $\beta_{\text{ion}}\approx0.84$ at the higher photon energy above the $N(1s)^{-1}$ *K* shell. We observe a more significant difference between the measured and computed β_{ion} values above the $O(1s)^{-1}$ threshold. The evolution is comparable for the two $NO^+(^3\Pi)$ and $NO^+(^1\Pi)$ ionic states in the calculation, although some differences are noticed.

TABLE II. Measured and computed β_{ion} and β_{el} asymmetry parameters for the total ionization including both the $^1\Pi$ and $^3\Pi$ channels.

	Experiment		Theory	
Energy (eV)	β_{ion}	β_{el}	β_{ion}	β_{el}
413.8	1.0±0.1	0.6±0.1	1.40	−0.43
415.7	1.0±0.1	0.7±0.1	1.49	0.24
418.3	0.6±0.1	1.2±0.1	0.84	1.01
550.5	0.7±0.1	0.8±0.1	1.27	0.285

The measured and computed β_{el} photoelectron asymmetry parameters also displayed in Table II are discussed in Sec. V B 2 in connection with the energy dependence of the $F_{LN}(\theta_e)$ functions.

2. Molecular frame photoemission: F_{LN} functions

As discussed in Sec. V A, the analysis of the $I(\theta_e,\phi_e,\chi,\gamma)$ distribution measured with elliptically polarized light provides the four $F_{LN}(\theta_e)$ functions ($F_{00},F_{20},F_{21},F_{22}$), the product s_3F_{11}, and the two Stokes parameters s_1 and s_2. In the present experiment we obtained $s_1\approx-0.44\pm0.04$ and $s_2\approx0\pm0.04$, leading to $s_3\approx0.9\pm0.05$ under the reasonable assumption of a degree of polarization of the light $P\approx1$. Figures 6(a)–6(d) display the five measured F_{LN} functions and the CDAD parameter for PI into $NO^+(^3\Pi$ and $^1\Pi)$ $N(1s)^{-1}$ at the photon excitation energies $h\nu\approx413.9$, 415.8, and 418.3 eV and $NO^+(^3\Pi$ and $^1\Pi)$ $O(1s)^{-1}$ at $h\nu\approx550.5$ eV, properly normalized to the computed PI cross section. All the F_{LN} functions exhibit a strong oscillatory structure corresponding to large polar angle emission anisotropies in the molecular frame. The significant amplitudes of F_{21} and F_{11} relative to F_{00} are the signature of a

TABLE III. Computed partial channel β_{ion} and β_{el} asymmetry parameters for the $^1\Pi$ and $^3\Pi$ channels.

	β_{ion}		β_{el}	
Energy (eV)	$^3\Pi$	$^1\Pi$	$^3\Pi$	$^1\Pi$
413.8	1.29	1.55	−0.50	−0.335
415.7	1.56	1.23	0.14	0.62
418.3	0.94	0.53	0.98	1.12
550.5	1.33	1.01	0.25	0.45

strong ($\phi_e=0°/\phi_e=180°$) azimuthal dependence of the electron emission pattern when the orientation of the molecule is tilted with respect to linearly polarized light, and ($\phi_e=90°/\phi_e=270°$) left-right asymmetry when the molecule perpendicular to the light propagation axis is photoionized by circularly polarized light, respectively. The measured circular dichroism is large and the CDAD parameter reaches significant values between −0.5 and +0.5. The positive value of F_{22} characterizes a Σ^+ (neutral initial state)$\rightarrow\Sigma^+$ (NO^+ ionic state), indicating that the 2π electron is a spectator in the $NO(^2\Pi)\rightarrow NO^+(^3\Pi$ or $^1\Pi)$ photoionization reaction.

The F_{LN} functions show progressive change with increasing photon energy above the $N(1s)^{-1}$ threshold. However, a drastic change is observed when comparing the $N(1s)^{-1}$ (c) and $O(1s)^{-1}$ (d) F_{LN} functions for the same photoelectron energy that display a strikingly quasisymmetric behavior. The F_{LN} functions for $O(1s)^{-1}$ ionization are very similar to those obtained for $N(1s)^{-1}$ ionization, changing the NO orientation, i.e., referring to the θ_e polar angle with respect to the O end of the molecule; as far as the dominant features are considered, they comply with the following relationships:

$$F_{00}^{O1s}(\theta_e) \approx F_{00}^{N1s}(\pi-\theta_e),$$

$$F_{20}^{O1s}(\theta_e) \approx F_{20}^{N1s}(\pi-\theta_e),$$

$$F_{22}^{O1s}(\theta_e) \approx F_{22}^{N1s}(\pi-\theta_e), \tag{8}$$

and

$$F_{21}^{O1s}(\theta_e) \approx -F_{21}^{N1s}(\pi-\theta_e),$$

$$F_{11}^{O1s}(\theta_e) \approx -F_{11}^{N1s}(\pi-\theta_e),$$

$$\mathrm{CDAD}^{O1s}(\theta_e) = -\mathrm{CDAD}^{N1s}(\pi-\theta_e). \tag{9}$$

Some deviations to this behavior are nevertheless observed, in particular, for the F_{11} function and the corresponding CDAD parameter. The inversion symmetry described in the relation above for F_{11} is satisfied in the $75°\leqslant\theta_e\leqslant180°$ range, whereas a different behavior is observed at lower emission angles.

The measured F_{LN} functions compare quite well with the MCSCI computed values at the four energies in Figs. 6(a)–6(d) with a larger amplitude of the oscillations for the computed F_{00} and F_{20} functions, when compared to the experimental result. The observed evolution of the circular dichroism as a function of the photon energy is very well predicted too. The most significant difference is found at the lowest photoelectron energy, in particular, for the F_{21} function where the first positive oscillation observed is not predicted by the calculations. We note that the $h\nu=413.9$ eV photon energy also corresponds to the region where the role of doubly excited states in the PI process has been invoked [16]: such autoionizing states are not included in the present calculations. In Figs. 6(a) and 6(c) the measurements are also compared with the theoretical results convoluted with the apparatus function using a Monte Carlo simulation of the experiment. The results of such simulation show that the effect of the instrumental widths is mainly to attenuate the amplitude of the oscillations of the computed F_{00} and F_{20}.

A comparison of the present results at the lower photon energy ($h\nu\approx413.9$ eV) with the four ($F_{00},F_{20},F_{21},F_{22}$) functions measured closer to the $N(1s)^{-1}$ threshold for $h\nu\approx412$ eV [18] shows very similar structures for the F_{LN} functions: the main differences are observed again for F_{21} at small values of θ_e and may be attributed to the energy dependence of the MFPADs near the threshold.

The β_{el} asymmetry parameter characterizes the photoelectron angular distribution with respect to linearly polarized light, which results from electron emission in the molecular frame integrated over the molecular axes orientation. It is interesting to note that, even if the structure and the relative importance of the F_{LN} functions are very well predicted by the calculations, which implies a good description of the main interactions governing the photoionization reaction, the β_{el} asymmetry parameter remains a sensitive parameter, which measures the cumulative effect of small differences in the F_{LN} functions. Table II shows that the β_{el} energy evolution is qualitatively well predicted, however, the measured

TABLE IV. Partial wave analysis of the $I_{\chi=0}(\theta_e)$ and $I_{\chi=90}(\theta_e)$ (averaged over ϕ_e) MFPADs in Legendre polynomial expansion for $N(1s)^{-1}$ (418.3 eV) and $O(1s)^{-1}$ (550.5 eV) PI reactions with A_0 normalized to 1; experimental results and statistical uncertainties (E), MCSCI calculations (T). For $O(1s)^{-1}$ PI the sign of the odd k values indicated in parentheses has been changed to allow for a "direct" comparison with the $N(1s)^{-1}$ PI analysis, according to the $\theta_e\rightarrow\pi-\theta_e$ inversion (see the text).

$I_{\chi=0}(\theta_e)$	A_1	A_2	A_3	A_4	A_5	A_6	A_7	A_8
$N(1s)^{-1}$ (E)	0.23±0.03	0.61±0.03	−0.13±0.04	−0.24±0.04	−0.65±0.05	1.02±0.05	−0.12±0.06	0.12±0.06
$N(1s)^{-1}$ (T)	0.16	0.30	−0.017	−0.56	−0.71	1.90	−0.11	−0.08
$O(1s)^{-1}$ (E)	(−)0.00±0.02	0.20±0.03	(−)0.68±0.03	−0.59±0.04	(−)0.24±0.04	1.09±0.05	(−)0.05±0.05	0.14±0.05
$O(1s)^{-1}$ (T)	(−)0.33	0.26	(−)0.80	−0.59	(+)0.45	1.55	(−)0.27	−0.05
$I_{\chi=90}(\theta_e)$								
$N(1s)^{-1}$ (E)	0.098±0.03	−0.39±0.03	−0.30±0.04	−0.62±0.04	0.16±0.05	0.14±0.05	0.11±0.06	−0.17±0.06
$N(1s)^{-1}$ (T)	−0.11	−0.25	−0.15	−0.8	0.27	0.052	−0.02	0.002
$O(1s)^{-1}$ (E)	(−)0.02±0.03	−0.23±0.04	(−)0.27±0.04	−0.80±0.05	(+)0.23±0.05	0.19±0.06	(+)0.12±0.06	−0.19±0.07
$O(1s)^{-1}$ (T)	(−)0.25	0.11	(−)0.18	−1.12	(+)0.44	0.02	(−)0.02	0.005

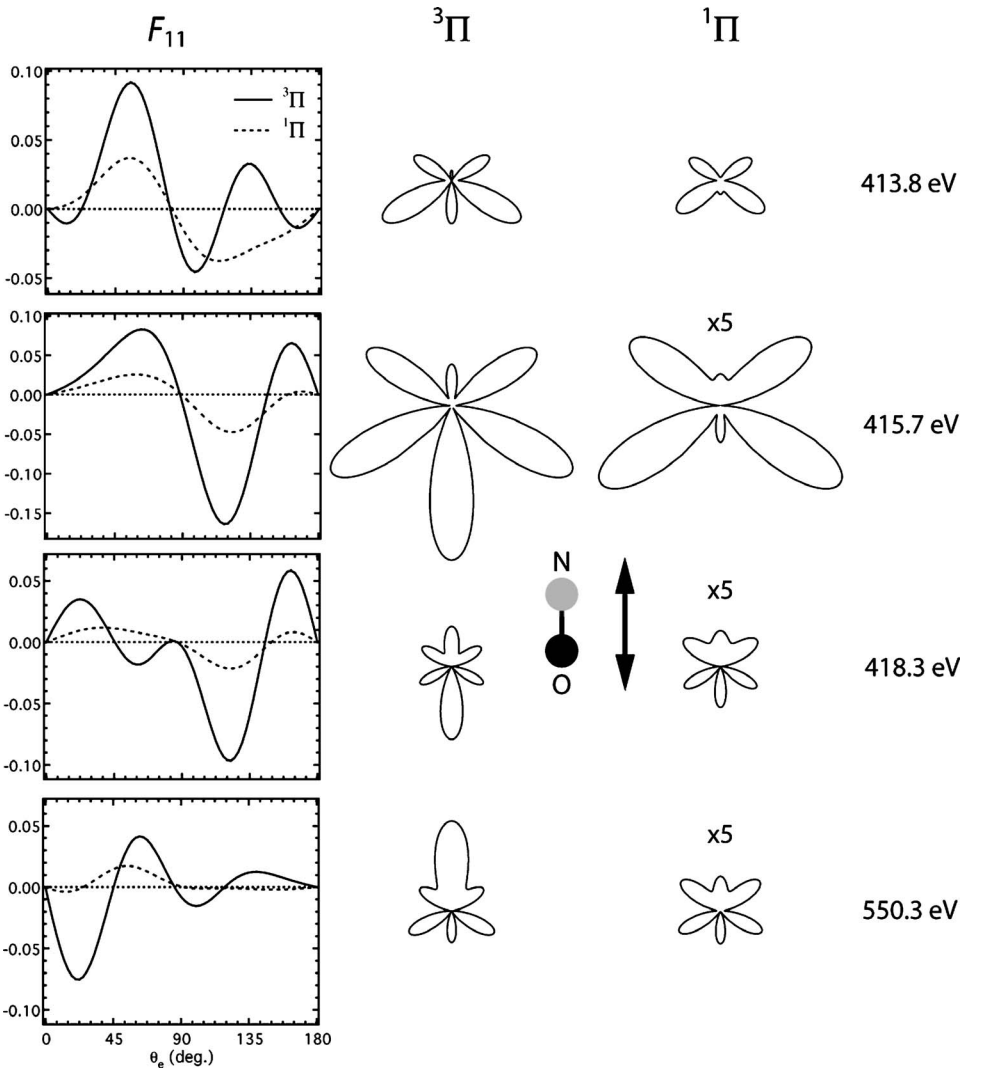

FIG. 9. Theoretical values of the multiplet-specific F_{11} functions in Mbarn (left panel), and polar plots of the $I_{\chi=0}(\theta_e)$ MFPADs for linearly polarized light in absolute scale (right panels), for the studied photon energies.

and computed values exhibit significant differences. This is especially true at low electron energies above the $N(1s)^{-1}$ threshold, where the measured β_{el} parameter is positive, and the computed β_{el} is negative for ionization into both multiplet states as seen in Table III. One may invoke different reasons that could be explored in forthcoming detailed experiments and calculations: Figure 2 shows that β_{el} changes rapidly at low energy so that a slight shift in the energy of the resonance can induce significant changes in the β_{el} value; vibrational averaging of the intermediate $NO^+(^3\Pi)$ or $NO^+(^1\Pi)$ ionic states has not been included in the present calculation; neither have the doubly excited states as mentioned above.

C. MFPAD observables: $I_\chi(\theta_e, \phi_e)$ distributions for $N(1s)^{-1}$ and $O(1s)^{-1}$ ionization

Figure 7 compares the $N(1s)^{-1}$ and $O(1s)^{-1}$ MFPADs for the photoelectron energy $E_e \approx 7$ eV, ($h\nu$=418.3 and 550.5 eV), using the 3D distributions of the measured (a) and computed (b) $I_\chi(\theta_e, \phi_e)$ MFPADs, for a molecule aligned parallel, perpendicular, at the magic angle with respect to linearly polarized light, and the MFPAD for a molecule aligned perpendicular to the propagation axis of circularly polarized light of helicity +1.

This representation illustrates the common features of the two $N(1s)^{-1}$ and $O(1s)^{-1}$ photoelectron angular distributions, as well as their remarkable "symmetric" behavior. In the case of parallel orientation, the emission of electrons is favored along the molecular axis in the direction of the atom, which has not been ionized [O for $N(1s)^{-1}$ ionization and N for $O(1s)^{-1}$ ionization], and displays two other maxima in the directions $\theta_e \approx 60°$ (120°) and $\theta_e \approx 120°$ (60°), respectively, pointing out the dominant role of $p\sigma$ and $f\sigma$ partial-wave channels. For the perpendicular orientation, electron emission is favored in the plane defined by the molecular and the polarization axes, in the directions $\theta_e \approx 60°$ (120°) and $\theta_e \approx 135°$ (45°), respectively, associated with the dominant role of the $p\pi$ and $d\pi$ partial waves. They display a mirrorlike structure with respect to the midpoint of a plane perpendicular to the NO molecular axis. For a molecule oriented at the magic angle with respect to linearly polarized light, and aligned perpendicular to the propagation axis of circularly polarized light of helicity +1, the MFPADs display more complex structures, and the symmetry transformation corresponds indeed to an inversion with respect to the emission

center. We point out that a similar behavior upon ionization of the C 1*s* and O 1*s* orbitals induced by linearly polarized light has been observed previously for the CO molecule [44].

The 1D plots in Fig. 8 represent the cuts of the $I_\chi(\theta_e,\phi_e)$ MFPADs discussed above for selected ϕ_e azimuthal angles, determined as explained in Sec. V A, Eq. (5). They enable a quantitative comparison between the experimental and theoretical results at the level of the MFPADs, complementary to the comparison of the $F_{LN}(\theta_e)$ functions in Sec. V B. Table IV displays the result of the partial-wave analysis of the measured and computed MFPADs for a molecule aligned parallel $I_{\chi=0}(\theta_e)$ or perpendicular $I_{\chi=90}(\theta_e)$ (after averaging over the ϕ_e azimuthal angle) to linearly polarized light. For these observables the angular distribution is expanded in terms of Legendre polynomials as $A_kP_k(\cos\theta_e)$, with k varying from 0 to $2l_{\max}$, where $l_{\max}$ is the largest angular momentum of the partial-wave channels significantly involved in the photoionization amplitudes. The expansion was limited to $k=8$ ($l_{\max}=4$) since contributions from higher ks were found to be negligible. Consistent with the $p\sigma$ and $f\sigma$ dominant character in the $I_{\chi=0}(\theta_e)$, Table IV shows the dominant contribution of the A_6 term in the expansion, with significant contributions of A_2, whereas A_4 is dominant for $I_{\chi=90}(\theta_e)$, consistent with the strong $d\pi$ character.

D. Multiplet state specific MFPADs: MCSCI results for ionization into the $NO^+(^3\Pi)$ and $(^1\Pi)$ ionic states

The analysis of the photoionization dynamics in terms of multiplet specific contributions assumes remarkable importance when resonant channels participate into the PI process [24,25]. Since the MFPADs change noticeably as the photon energy sweeps the region around the maximum of a resonance [24,25], accurate knowledge of the corresponding peak position is essential for a correct interpretation of the experimental data. This sensitivity to resonance energy was shown in the case of core $N(1s)^{-1}$ PI of NO [13,14].

Figure 9 summarizes the contributions of $^3\Pi$ and $^1\Pi$ channels to the MFPADs computed at the studied photon energies for the dominant parallel transition, $I_{\chi=0}(\theta_e)=F_{00}(\theta_e)+F_{20}(\theta_e)$ [Eq. (5)], along with the predicted F_{11} functions. As mentioned previously the contribution of the $^3\Pi$ channel dominates that of the $^1\Pi$ channel and thus generally controls the spatial distributions of the photoelectrons. It may be observed that the MFPADs for the $N(1s)^{-1}$ ($^3\Pi$) channel evolve significantly as the photoelectron energy is sampled across the σ^* shape resonance located around 415 eV. Such a variation is manifested in the profiles of the corresponding F_{11} functions. As a matter of fact, the F_{11} computed at high energy resembles the low-energy F_{11} after inversion through the center ($\theta_e=90°$), i.e., $F_{11}(\theta_e;E=418.3\text{ eV})$ is comparable to $-F_{11}(\pi-\theta_e;E=413.8\text{ eV})$, and this reflects the change of approximately π radians in the phases of the PI matrix elements for the parallel transition, which occurs as the energy passes through the σ^*-shape resonance [4,45]. The $N(1s)^{-1}$ ($^1\Pi$) channel does not display such an inversion symmetry in the studied energy range, despite the σ^* resonant state being formed by a linear combination of both $^3\Pi$ and $^1\Pi$ ionic states. This may be the result of the σ^*-shape resonance occurring for the $^1\Pi$ channel at lower energy than for the $^3\Pi$ one (Fig. 2), bringing the lowest energy measurement so close to the top of the peak—centered at about 414.4 eV—that the phase change and the related differences are reduced. Once again, this stresses the high sensitivity of the MFPADs in probing for both presence and position of shape resonant states in experimental investigations on molecular photoionization. We note that some discrepancies have already been found for the NO $N(1s)^{-1}$ ($^1\Pi$) channel in the comparison of multiplet-specific MFPADs measured earlier at comparable photoelectron KEs with the results of MCSCI calculations performed using single-center spherical functions with $l_{\max}=60$ and theoretical photoionization thresholds [13]. This has been tentatively attributed to a participation of autoionization channels, which are not included in the theory and cannot be accounted for separately in the experiment, as well as vibrational effects that may affect to a larger extent the weakest channel. The theoretical polar plots for the $^1\Pi$ channel obtained here and shown in Fig. 9 seem to confirm overall the results of the previous MCSCI calculations.

The MFPADs for $O(1s)^{-1}$ PI correspond to photoelectrons emitted with approximately the same KE ($\approx$7 eV) as the ones of the high-energy MFPADs for $N(1s)^{-1}$. While the $^1\Pi$ channel still plays a minor role, the photoelectron distribution of the $O(1s)^{-1}$ ($^3\Pi$) channel appears to be almost the mirror image of the one of the $N(1s)^{-1}$ ($^3\Pi$) channel at 418.3 eV with respect to the midpoint of the molecular axis, consistent with the discussion in Sec. V B 2. This is emphasized in the profiles of the F_{11} functions, which satisfy qualitatively the inversion symmetry properties, in particular, in the $75°\leqslant\theta_e\leqslant180°$ range. This behavior may be attributed to the strong atomic character of both the 1σ (O 1*s*) and 2σ (N 1*s*) molecular orbitals in NO: the corresponding wave functions are strongly localized and very close in shape to the original 1*s* atomic orbitals of similar size. This would bring to dipole matrix elements of comparable value. Thus one may expect the scattering dynamics of the photoelectrons emitted from N and O centers to be similar, within the rough approximation that considers the effects of the molecular scattering potential on the photoelectron waves to be the same in both cases, as those core orbitals are well separated in energy from the valence ones. To investigate this point in further detail, the magnitudes d_{lm} and the absolute phases τ_{lm} of the principal dipole matrix elements for parallel transitions involved in the $N(1s)^{-1}$ ($^3\Pi,^1\Pi$) and $O(1s)^{-1}$ ($^3\Pi,^1\Pi$) photoionization channels have been compared in the case of similar photoelectron KE, i.e., at the photon energies of 418.3 and 550.3 eV, respectively ($E_e\approx7$ eV for the $^3\Pi$ states, $E_e\approx5.5$ and 6.5 eV for the $N(1s)^{-1}$ and $O(1s)^{-1}$ $^1\Pi$ states, respectively). The results are summarized in Fig. 10. The agreement between the magnitudes as well as the phases of the dipole matrix elements describing the $N(1s)^{-1}$ and the $O(1s)^{-1}$ photoionization is remarkable in both the channels considered. These results confirm at the highly accurate level of theory provided by the present MCSCI calculations the assumption of a comparable PI dynamics for both 1σ (O 1*s*) and 2σ (N 1*s*) molecular orbital ionization. The MFPADs are very similar when the ionized center is taken as

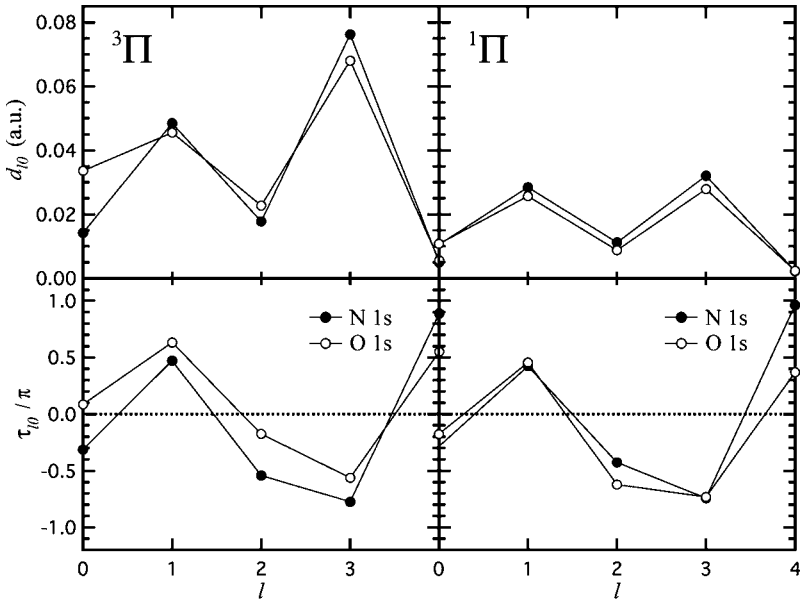

FIG. 10. Computed magnitudes (a.u.) and absolute phases (multiple of π radians) of the principal PI dipole matrix elements involved in the $N(1s)^{-1}$ ($^3\Pi, ^1\Pi$) and $O(1s)^{-1}$ ($^3\Pi, ^1\Pi$) processes, at the photon energies of 418.3 eV and 550.3 eV for $N(1s)^{-1}$ and $O(1s)^{-1}$ ionization, respectively.

a reference for the orientation of the molecular axis, then they correspond to one another by the transformation $\theta_e \rightarrow \pi - \theta_e$, and subsequent changes in the F_{LN} functions, when the molecular axis orientation is chosen to be identical for both reactions. It has been pointed out earlier that the dominance of the $f\sigma$ and $p\sigma$ odd-parity partial waves for $N(1s)^{-1}$ photoionization may be attributed to the fact that the parent ion $N(1s)^{-1}$ NO^+ has the equivalent core with the O_2^+ molecule, implying a weak coupling between odd-parity and even-parity continua because of the inversion symmetry [13]. This may actually be verified in Fig. 11 where only the s wave in the $^1\Pi$ channel carries a non-negligible contribution at low photon energy. A detailed inspection of Fig. 10 shows that this dominance is somewhat attenuated for $O(1s)^{-1}$ photoionization where the equivalent core approximation gives the asymmetric NF^+ core. In particular, we note the enhanced $l=0$ matrix element in the $O(1s)^{-1}$ $^3\Pi$ channel compared to the corresponding matrix element in the $N(1s)^{-1}$ channel.

In order to understand the nature of the $\sigma \rightarrow \sigma^*$-shape resonances occurring in the $N(1s)^{-1}$ and $O(1s)^{-1}$ photoionization continua, the contribution of each partial-wave channel has been analyzed for the σ symmetry ($m=0$) in terms of the square modulus of the dipole transition elements d_{lm} for both $^3\Pi$ and $^1\Pi$ channels. Only partial waves with l up to 4 have been retained into the analysis, since contributions from higher ls have been found to be negligible. The d_{lm} have been renormalized such that the sum $d_{00}^2+d_{10}^2+d_{20}^2+d_{30}^2+d_{40}^2$ is equal to the partial cross section for the channel considered. The results for $N(1s)^{-1}$ photoionization are summarized in Fig. 11. It is clear that the f partial wave (d_{30}^2) dominates at all the photon energies considered in the NO $N(1s)^{-1}$ ($^3\Pi$) channel, followed by the p-wave contribution d_{10}^2. This agrees only in part with what was estimated by Hosaka *et al.* [13] on the basis of their experimental observations, as their data suggested that emission into p partial waves prevails at the low-energy side of the shape resonance. On the other hand, the present analysis of the NO $N(1s)^{-1}$ ($^1\Pi$) channel is consistent with the mentioned experimental estimates, showing the p waves to carry the main contribution, while the f waves become more and more important as we move across the shape resonance up to the point where d_{30}^2 become comparable with d_{10}^2. This competitive tunneling through the l

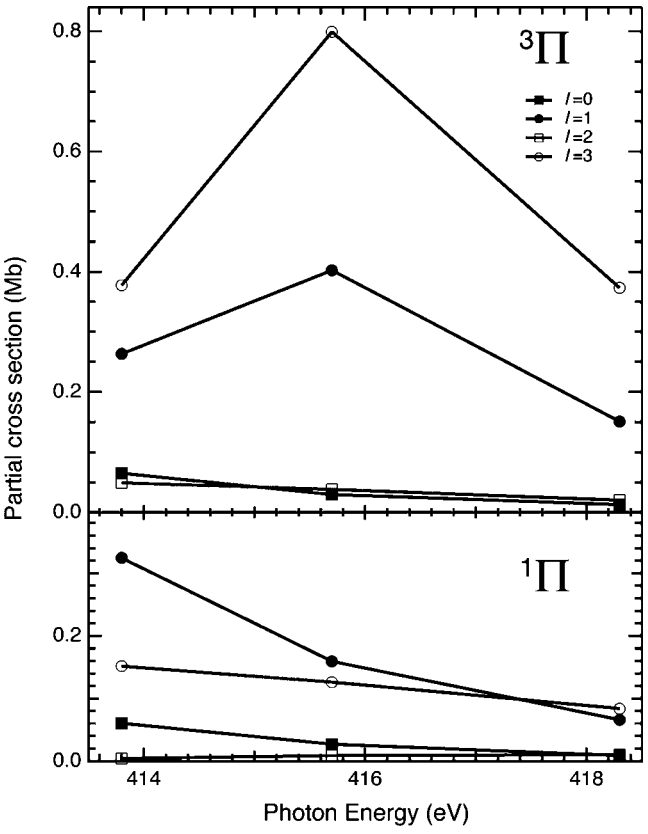

FIG. 11. Principal partial wave contributions to the N $1s \rightarrow \varepsilon\sigma$ cross section reported in terms of the square modulus of the corresponding dipole matrix element d_{l0}^2 predicted at each energy studied. The sum $d_{00}^2+d_{10}^2+d_{20}^2+d_{30}^2+d_{40}^2$ has been renormalized to the corresponding partial cross sections of each channel.

$=3$ and $l=1$ angular momentum barriers makes the predicted photoelectron dynamics of the $^1\Pi$ channel richer than that of the $^3\Pi$ channel. At the photon energy of 550.3 eV, the partial-wave analysis of NO $O(1s)^{-1}$ photoionization shows that the contribution of the f waves exceeds the contribution of p waves with d_{30}^2/d_{10}^2 ratios of 2.23 for the $^3\Pi$ channel and 1.18 for the $^1\Pi$ one. Note in the $N(1s)^{-1}$ case at 418.3 eV and in the $O(1s)^{-1}$ case at 550.3 eV, the $l=3$ to $l=1$ ratios are close to 1.0 in the ionization leading to the $^1\Pi$ ion states. In contrast, the $l=3$ to $l=1$ ratios are significantly larger than 1.0 in the ionization to the corresponding $^3\Pi$ ion states.

VI. CONCLUSION

The vector correlation method, including both the experimental approach based on ion-electron three-dimensional velocity imaging and the related theory of measurement, has been extended to investigate **K**-shell photoionization of linear molecules at the BESSY third generation synchrotron radiation facility, using elliptically polarized light. In this paper we have focused on the determination of the MFPADs for $N(1s)^{-1}$ and $O(1s)^{-1}$ ionization of the NO molecule at selected photon energies in the shape resonance region, derived from the analysis of the $(\mathbf{V}_N, \mathbf{V}_O, \mathbf{V}_e, \hat{\mathbf{e}})$ vector correlation when photoionization is followed by one electron Auger decay. The measured MFPADs are reported for the sum of the PI reactions into the $NO^+(^3\Pi)$ and $NO^+(^1\Pi)$ ionic states, dominated by the triplet state channel, in two forms: (i) the set of the five one-dimensional $F_{LN}(\theta_e)$ functions, and (ii) $I_\chi(\theta_e, \phi_e)$ the polar and azimuthal angle distributions for selected orientations of the molecular axes and for specific azimuthal angles. The MFPADs display significant emission anisotropies, and a large molecular frame circular dichroism, evolving progressively with the photon energy across the shape resonance, and displaying a clear inversion symmetry between the $N(1s)^{-1}$ and $O(1s)^{-1}$ ionized sites. The experimental results are in fairly good agreement with recent MCSCI calculations. Significant possible sources of the remaining discrepancies between experiment and theory include the lack of vibrational averaging in the calculations and the limited inclusion of correlation in the wave functions used to compute the cross sections. The limitations in the correlation treatment include both the limited configuration expansions and limited orbital sets used in the calculations of initial and final bound states as well as the use of only two channels in the scattering wave function. The limitations in the bound state wave functions were particularly noted in the sensitivity of the computed results to the choice of the orbital set used. The set used in the calculations presented here were obtained from an MCSCF calculation on the ground state of NO^+ and was chosen since it gave better agreement with experiment for the position of the shape resonance than the other orbital sets that were tested. These theoretical results provide complementary knowledge about the multiplet specific molecular photoemission reactions, and give access to the dipole matrix elements of the PI reactions. They confirm the dominant role of coherent p and f partial waves in the electronic continuum, and support a simple interpretation of the relationship between the $N(1s)^{-1}$ and $O(1s)^{-1}$ MFPADs. They motivate further experimental effort in the study of the photoionization dynamics of multiplet specific reactions. Concerning the Auger decay process, the analysis of the photoelectron-ion-ion kinetic energy correlation, combined with other spectroscopic studies of the NO^{2+} molecular dication, provides complementary information about the populated NO^{2+} ionic states and related dissociation channels.

ACKNOWLEDGMENTS

We gratefully acknowledge M. Lebech for extending the acquisition software to the multi-ion detection. We are grateful to T. Kachel, beamline scientist (UE 56 PGM-1) at BESSY, and B. Pilette (SOLEIL, France) for his technical support. We acknowledge the support through the BESSY IA-SFS program (Contract No. RII 3CT-2004-506008), as well as through a PICS France—USA CNRS contract. R.R.L. gratefully acknowledges the support from the Japanese Society for the Promotion of Science and the hospitality of K. Ueda and the Tohoku University. R.R.L. and R.M. also acknowledge the support of the Robert A. Welch Foundation (Houston, Texas) under Grant No. A-1020 and the Chemical Sciences, Geosciences and Biosciences Division, Office of Basic Energy Sciences, Office of Science, U.S. Department of Energy.

[1] D. Dowek, in *Many-Particle Quantum Dynamics in Atomic and Molecular Fragmentation*, edited by J. Ullrich and V. P. Shevelko (Springer, Berlin, 2003), and references therein.

[2] A. Lafosse, M. Lebech, J. C. Brenot, P. M. Guyon, O. Jakutzki, L. Spielberger, M. Vervloet, J. C. Houver, and D. Dowek, Phys. Rev. Lett. **84**, 5987 (2000).

[3] R. R. Lucchese, A. Lafosse, J. C. Brenot, P. M. Guyon, J. C. Houver, M. Lebech, G. Raseev, and D. Dowek, Phys. Rev. A **65**, 020702 (2002).

[4] M. Lebech, J. C. Houver, A. Lafosse, C. Alcaraz, L. Nahon, R. R. Lucchese, and D. Dowek, J. Chem. Phys. **118**, 9653 (2003).

[5] M. Lebech, J. C. Houver, and D. Dowek, Rev. Sci. Instrum. **73**, 1866 (2002).

[6] D. Dill, J. Chem. Phys. **65**, 1130 (1976); N. A. Cherepkov and V. V. Kuznetsov, Z. Phys. D: At., Mol. Clusters **7**, 271 (1987); N. A. Cherepkov and G. Raseev, J. Chem. Phys. **103**, 8283 (1995).

[7] T. Jahnke, Th. Weber, A. L. Landers, A. Knapp, S. Schössler, J. Nickles, S. Kammer, O. Jagutzki, L. Schmidt, A. Czasch, T. Osipov, E. Arenholz, A. T. Young, R. Diez Muino, D. Rolles, F. J. Garcia de Abajo, C. S. Fadley, M. A. Van Hove, S. K. Semenov, N. A. Cherepkov, J. Rösch, M. H. Prior, H. Schmidt-Böcking, C. L. Cocke, and R. Dörner, Phys. Rev. Lett. **88**, 073002 (2002).

[8] S. Motoki, J. Adachi, K. Ito, K. Ishii, K. Soejima, A. Yagishita, S. K. Semenov, and N. A. Cherepkov, Phys. Rev. Lett. **88**, 063003 (2002).
[9] O. Gessner, Y. Hikosaka, B. Zimmermann, A. Hempelmann, R. R. Lucchese, J. H. D. Eland, P. M. Guyon, and U. Becker, Phys. Rev. Lett. **88**, 193002 (2002).
[10] N. Kosugi, J. I. Adachi, E. Shigemasa, and A. Yagishita, J. Chem. Phys. **97**, 8842 (1992).
[11] P. Lin and R. R. Lucchese, J. Synchrotron Radiat. **8**, 150 (2001).
[12] K. Hosaka, J. Adachi, M. Takahashi, and A. Yagishita, J. Phys. B **36**, 4617 (2003).
[13] K. Hosaka, J. Adachi, M. Takahashi, A. Yagishita, P. Lin, and R. R. Lucchese, J. Phys. B **37**, L49 (2004).
[14] A. Rüdel, U. Hergenhahn, K. Maier, E. E. Rennie, O. Kugeler, J. Viefhaus, P. Lin, R. R. Lucchese, and A. M. Bradshaw, New J. Phys. **7**, 189 (2005), and references therein.
[15] G. Remmers, M. Domke, A. Puschmann, T. Mandel, G. Kaindl, E. Hudson, and D. A. Shirley, Chem. Phys. Lett. **214**, 241 (1993).
[16] S.-W. Yu, W. C. Stolte, R. Guillemin, G. Öhrwall, I. C. Tran, M. N. Piancastelli, R. Feng, and D. W. Lindle, J. Phys. B **37**, 3583 (2004), and references therein.
[17] K. Hosaka, J. Adachi, A. V. Golovin, M. Takahashi, N. Watanabe, and A. Yagishita, Jpn. J. Appl. Phys., Part 1 **45**, 1841 (2006).
[18] N. Saito, X. J. Liu, Y. Morishita, I. H. Suzuki, and K. Ueda, J. Electron Spectrosc. Relat. Phenom. (to be published).
[19] W. B. Li, J. C. Houver, A. Haouas, F. Catoire, C. Elkharrat, R. Guillemin, L. Journel, R. Montuoro, R. R. Lucchese, M. Simon, and D. Dowek, J. Electron Spectrosc. Relat. Phenom. (to be published).
[20] M. Richard-Viard, A. Delboulbé, and M. Vervloet, Chem. Phys. **209**, 159 (1996).
[21] M. R. Weiss, R. Follath, K. J. S. Sawhney, F. Senf, J. Bahrdt, W. Frentrup, A. Gaupp, S. Sasaki, M. Scheer, H. C. Mertins, D. Abramsohn, F. Schäfers, W. Kuch, and W. Mahler, Nucl. Instrum. Methods Phys. Res. A **467**, 449 (2001); K. J. S. Sawhney, F. Senf, M. Scheer, F. Schäfers, J. Bahrdt, A. Gaupp, and W. Guddat, *ibid.* **390**, 395 (1997).
[22] Roentdek-Handels GmbH, Kelkheim, Germany.
[23] IPNO "Détection: Temps, Position, Image," Technology Division (supported by the Mission Ressources et Compétences Technologiques-CNRS Federation FR2764 and by the Université Paris-Sud).
[24] R. E. Stratmann and R. R. Lucchese, J. Chem. Phys. **102**, 8493 (1995).
[25] R. E. Stratmann, R. W. Zurales, and R. R. Lucchese, J. Chem. Phys. **104**, 8989 (1996).
[26] R. R. Lucchese, K. Takatsuka, and V. Mc Koy, Phys. Rep. **131**, 147 (1986).
[27] K. P. Huber and G. Herzberg, *Molecular Spectra and Molecular Structure IV. Constant of Diatomic Molecules* (Van Nostrand-Reinhold, New York, 1979).
[28] T. H. Dunning, Jr., J. Chem. Phys. **90**, 1007 (1989).
[29] P. van der Straten, R. Morgenstern, and A. Niehaus, Z. Phys. D: At., Mol. Clusters **8**, 35 (1988).
[30] J. H. D. Eland, S. S. W. Ho, and H. L. Worthington, Chem. Phys. **290**, 27 (2003).
[31] I. H. Suzuki and N. Saito, Laser Chem. **16**, 5 (1995).
[32] T. Masuoka, J. Chem. Phys. **100**, 6422 (1994).
[33] D. Edvardsson, M. Lundqvist, P. Baltzer, B. Wannberg, and S. Lunell, Chem. Phys. Lett. **256**, 341 (1996).
[34] L. G. M. Pettersson, L. Karlsson, M. P. Keane, A. Naves de Brito, N. Correia, M. Larsson, L. Broström, S. Mannervik, and S. Svensson, J. Chem. Phys. **96**, 4884 (1992).
[35] W. E. Moddeman, T. A. Carlson, M. O. Krause, and B. P. Pullen, J. Chem. Phys. **55**, 2317 (1971).
[36] H. Agren, J. Chem. Phys. **75**, 1267 (1981).
[37] D. L. Cooper, Chem. Phys. Lett. **132**, 377 (1986).
[38] W. B. Li *et al.* (unpublished).
[39] R. N. Zare, J. Chem. Phys. **47**, 204 (1967); Mol. Photochem. **4**, 1 (1972).
[40] D. Dowek, M. Lebech, J. C. Houver, and R. R. Lucchese, J. Electron Spectrosc. Relat. Phenom. **141**, 211 (2004).
[41] Th. Weber *et al.*, J. Phys. B **34**, 3669 (2001).
[42] M. Lebech, J. C. Houver, D. Dowek, and R. R. Lucchese, J. Chem. Phys. **117**, 9248 (2002).
[43] N. Saito and I. H. Suzuki, Phys. Rev. A **43**, 3662 (1991).
[44] T. Jahnke, Th. Weber, T. Osipov, A. L. Landers, O. Jagutzki, L. Ph. H. Schmidt, C. L. Cocke, M. H. Prior, H. Schmidt-Böcking, and R. Dörner, J. Electron Spectrosc. Relat. Phenom. **141**, 229 (2004).
[45] A. U. Hazi, Phys. Rev. A **19**, 920 (1979).